

2018

Influence of Natural Convection During Dendritic Array Growth of Metal Alloys (Gradient Freeze Directional Solidification)

Suyog N. Mahajan
Cleveland State University

Follow this and additional works at: <https://engagedscholarship.csuohio.edu/etdarchive>

 Part of the [Chemical Engineering Commons](#)

How does access to this work benefit you? Let us know!

Recommended Citation

Mahajan, Suyog N., "Influence of Natural Convection During Dendritic Array Growth of Metal Alloys (Gradient Freeze Directional Solidification)" (2018). *ETD Archive*. 1074.

<https://engagedscholarship.csuohio.edu/etdarchive/1074>

This Thesis is brought to you for free and open access by EngagedScholarship@CSU. It has been accepted for inclusion in ETD Archive by an authorized administrator of EngagedScholarship@CSU. For more information, please contact library.es@csuohio.edu.

INFLUENCE OF NATURAL CONVECTION DURING DENDRITIC ARRAY
GROWTH OF METAL ALLOYS
(GRADIENT FREEZE DIRECTIONAL SOLIDIFICATION)

SUYOG MAHAJAN

Bachelor of Science in Chemical Engineering

University of Pune

MAY 2015

Submitted in partial fulfillment of requirements for the degree

MASTER OF SCIENCE IN CHEMICAL ENGINEERING

at the

CLEVELAND STATE UNIVERSITY

AUGUST 2018

We hereby approve this thesis for

SUYOG N MAHAJAN

Candidate for the Master of Science in Chemical Engineering degree for the

Department of Chemical and Biomedical Engineering

and CLEVELAND STATE UNIVERSITY'S

College of Graduate Studies

Dissertation Chairperson, Surendra Tewari, Ph.D.

Department of Chemical & Biomedical Engineering

Department & Date

Dissertation Committee Member, Orhan Talu, Ph.D.

Department of Chemical & Biomedical Engineering

Department & Date

Dissertation Committee Member, Jorge E Gatica, Ph.D.

Department of Chemical & Biomedical Engineering

Department & Date

Dissertation Committee Member, Kiril A Streletzky, Ph.D.

Department of Physics, Cleveland State University

Department & Date

Student's Date of Defense: September 06, 2018

ACKNOWLEDGEMENTS

Foremost, I would like to express my sincere gratitude to my advisor Prof. Surendra Tewari for the continuous encouragement and support of my Masters' research. I am extremely indebted for his motivation, patience and enormous knowledge. His guidance has always been crucial throughout my research and writing of this thesis. The amount of learning and great exposure that I received during my span as a Graduate Research Assistant will always be cherished by me all my life.

Besides my advisor, I would like to thank the rest of my thesis committee: Prof. Orhan Talu, Prof. Jorge E Gatica, Prof. Kiril A Strelitzky, for taking out time to read my thesis and for being supportive through their encouragement, and perceptive comments.

My sincere thanks also go to all Professors from Chemical and Biomedical Engineering Department as I have tried implementing whatever I learnt through them by means of courses. I am thankful to Darlene and Becky for their continual support and making things very comfortable. Without your support, it would be really difficult to get through administrative things so easily.

I thank my fellow lab mates in Materials Research group for the stimulating discussions. Also, I thank my other classmates, my roommates and other friends in Cleveland who have played great role in making my stay in Cleveland beautiful.

Last but not the least, I would like to thank my family: my parents Nathu Mahajan and Sunita Mahajan, for being the constant source of inspiration throughout my life and believing in me. This accomplishment would have not been possible without them.

Finally, I would like to thank NASA for funding this project.

INFLUENCE OF NATURAL CONVECTION DURING DENDRITIC ARRAY
GROWTH OF METAL ALLOYS
(GRADIENT FREEZE DIRECTIONAL SOLIDIFICATION)

SUYOG MAHAJAN

ABSTRACT

Purpose of this study was to examine the microstructural evolution of primary dendrites during “Gradient Freeze DS process” in cylindrical Pb-5.8% Sb alloy samples to generate the ground- based research data to support a future microgravity experiment on the Space Station in a convection free environment. Pb-5.8Sb was selected for this study because of its ease of processing and availability of physical property data which will be required for predicting the dendrite morphology parameters, such as, primary dendrite spacing and dendrite trunk diameter. This alloy is also susceptible to thermosolutal convection caused by density inversion of the met in the mushy-zone during DS with melt on top and solid below (gravity pointing down). Two furnace cooling rates, 0.5 C/min and 4 C/min were utilized during the gradient freeze DS. Morphology of primary dendrites was observed to change from being branch-less (cellular) in the very beginning of DS, to those showing onset of side-branching, and finally to well-branched tree-like structure having tertiary and higher level side-branches as the solidification progressed from the cold to the hot end of the samples. Extensive macrosegregation was observed along the DS length, initially being solute poor and then becoming more and more solute rich as the solidification progressed. Experimentally observed primary spacings are smaller and the trunk diameter larger than those predicted from theoretical models which assume purely diffusive transport during solidification.

TABLE OF CONTENTS

	Page
ABSTRACT	iv
LIST OF TABLES	viii
LIST OF FIGURES	ix
CHAPTER	
I INTRODUCTION	1
1.1 Directional Solidification (DS) of alloys	1
1.1.1. Directional Solidification Methods.....	4
1.1.1.1. <i>Steady State DS</i>	4
1.1.1.2. <i>Gradient freeze directional solidification</i>	5
1.2. Convection During Directional Solidification	5
1.2.1. Thermally and Solutally Stabilizing Growth	5
1.2.2. Thermally Stabilizing, but Solutally Destabilizing Growth	6
1.3. Convection and Dendrite Array Morphology	7
1.4. Theoretical Models to Describe Primary Dendrite Morphology	9
1.4.1. Primary Dendrite Nearest Neighbor Spacing Hunt-Lu [18] Model.....	10
1.4.2. Primary Dendrite Trunk Diameter Model.....	11
II PURPOSE OF THIS RESEARCH	12
III EXPERIMENTAL AND ANALYTICAL PROCEDURES	14
1.1. Alloy selection.....	14
1.2. Gradient Freeze DS Equipment and Procedure.....	16
1.3. Specimen preparation (transverse sections) and metallography	18

1.3.1.	Cutting, Mounting, And Polishing.....	19
1.3.2.	Optical Microscopy.....	21
1.3.3.	Montage Making and Image Analysis	21
1.3.4.	Dendrite Trunk Diameter	23
1.3.5.	Primary Dendrite Spacing.....	24
1.3.5.1.	Nearest Neighbor Spacing.....	24
1.3.5.2.	Minimum Spanning Tree	25
1.3.6.	Fraction Eutectic	25
1.3.6.1.	Thresholding.....	25
1.3.6.2.	Watershed.....	27
1.3.6.3.	Particle Size Cut-Off.....	28
1.3.6.4.	Fraction Eutectic Calculation	28
IV	RESULTS AND DISCUSSION.....	30
4.1.	Dendrite Morphology Variations During Gradient Freeze DS	30
4.1.1.	Gradient Freeze DS at Slow Cooling Rate	30
4.1.2.	Gradient Freeze DS at Fast Cooling Rate.....	33
4.2.	Thermal Gradient and Growth Speed Variation Along DS length	37
4.2.1.	High Cooling Rate Sample (sample ID: 11_6_17).....	38
4.2.2.	Slow Cooling Rate Sample (sample ID: 12_11_17).....	45
4.3.	Dependence of the solidification behavior as a function of furnace cooling rate during gradient freeze DS process.	53
4.4.	Macrosegregation along the DS length	56
4.5.	Comparison with Theoretical Predictions	59

4.5.1.	Minimum Spanning Tree Spacing	59
4.5.2.	Nearest Neighbor Spacing (NNS).....	63
4.5.3.	Trunk Diameter (TD).....	65
V	SUMMARY	67
	REFERENCES	70

LIST OF TABLES

Table	Page
1 Thermophysical properties of Pb–5.8 wt. pct. Sb used to calculate predict primary dendrite spacing and trunk diameter.	15
2 Growth conditions of two Pb–5.8 Sb samples examined in this study.....	18
3 Polishing procedure for 9-mm to 12.7-mm diameter sections sample preparation	20
4 Comparison of dendrite morphology variation with respect to distance for slower and faster cooling rate sample.....	36
5 Locations of transverse samples and the times when the eutectic and liquidus isotherms arrived at those locations (# 11_6_17).	40
6 Mushy zone freezing rate with respect to distance for transverse samples cut from #11_6_17	42
7 Growth speed of the eutectic and liquidus isotherms vs. distance of the cross-sections with respect to TE at the onset of DS for #11_6_17	43
8 Values of Thermal gradient with respect to distances of transverse samples (#11_6_17).	44
9 Locations of transverse samples and the times when the eutectic and liquidus isotherms arrived at those locations (#12_11_17).....	47
10 Values of Mushy zone cooling rate with respect to distance for 12_11_17	49
11 Growth speed of the eutectic and liquidus isotherms vs. distance of the cross-sections with respect to TE at the onset of DS for #12_11_17.....	50
12 Values of Thermal gradient with respect to distance for 12_11_17	52

LIST OF FIGURES

Figure	Page
1. Succinonitrile – 9 wt. % Water “Transparent alloy” directionally solidified ($\sim 5\mu\text{m s}^{-1}$, $\sim 30\text{Kcm}^{-1}$) (Dr. Grugel, NASA-MSFC)	2
2. Transverse view of, (a) Side Arms of Primary Dendrite in DSed Pb-5.8 Sb alloy and (b) Secondary, tertiary, and higher order branches in a typical DSed Pb-5.8 Sb alloy.	3
3. Schematic of steady state directional solidification.....	4
4. Schematic of gradient freeze directional solidification	5
5. Schematic Temperature, Concentration and Density Profiles in inter-dendritic Liquid, Al-Cu	6
6. Schematic Temperature, Concentration and Density Profiles in inter-dendritic Liquid, Pb-Sb ⁸	7
7. Image of transverse slice of an Al-19 % Cu alloy, grown at $10\ \mu\text{m s}^{-1}$ ⁷ . This depicts an example of transverse phase macrosegregation.....	8
8. Image of transverse slice of a Pb-6 % Sb alloy. This depicts an example of channel formation because of plume type thermos-solutal convection.....	9
9. Pb-Sb Phase Diagram [20].....	15
10. Gradient Freeze DS facility and process. (a) Gradient Zone DS facility (b) Detailed image of the heat extracting gallium bath at the bottom, (c) typical quartz crucible in this research showing the locations where chromel-alumel thermocouples were attached on its outer surface, (d) Locations of the thermocouple tips as a function of distance from the initial location of T_E at the onset of DS.....	18
11. Temperature profile recorded by ten thermocouples located at known separation distances as a function of processing time for a typical gradient-freeze DS at a 4 C/min furnace cooling rate.....	19
12. Screen capture of bounding rectangle measurement for trunk diameter	24
13. Minimum Spanning Tree for a directionally solidified Pb-5.8 Sb alloy microstructure.	25

14. Typical example depicting the thresholding procedure of an 8-bit image of an Pb-Sb transverse slice with corresponding intensity histograms.	27
15. Typical example depicting the watershed and particle area cut-off procedure of a binary image.	28
16. Transverse microstructure of 12_11_17 at different distance away from Te (a) 0.25 cm (b) 0.75 cm (c) 1.75 cm (d) 2.75 cm (e) 3.75 cm (f) 4.75 cm (g) 5.75 cm (h) 6.75 cm (i) 7.75 cm (j) 8.75 cm (k) 9.75 cm (l) 10.75 cm (m) 11.75 cm (n) 12.75 cm (o) 13.75 cm	32
17. Transverse microstructure of 12_11_17 at different distance away from Te (a) 0.25 cm (b) 0.75 cm (c) 1.75 cm (d) 2.75 cm (e) 3.75 cm (f) 4.75 cm (g) 5.75 cm (h) 6.75 cm (i) 7.75 cm (j) 8.75 cm (k) 9.75 cm (l) 10.75 cm (m) 11.75 cm (n) 12.75 cm (o) 13.75 cm	33
18. Transverse microstructure of 11_6_17 at different distance away from Te (a) 0.5 cm (b) 1 cm (c) 2 cm (d) 3 cm (e) 4 cm (f) 5 cm (g) 6 cm (h) 7 cm (i) 8 cm (j) 9 cm (k) 10 cm (l) 11 cm (m) 12 cm.....	35
19. Transverse microstructure of 11_6_17 at different distance away from Te (a) 0.5 cm (b) 1 cm (c) 1 cm (d) 3 cm (e) 4 cm (f) 5 cm (g) 6 cm (h) 7 cm (i) 8 cm (j) 9 cm (k) 10 cm (l) 11 cm (m) 12 cm.....	36
20. Temperature along the sample length with respect to time for # 11_6_17 sample. ...	39
21. Temperature variation from 290 C (C above the liquidus) to 250 C (C below the eutectic) as a function of time for sample # 11_6_17	39
22. Distance of eutectic and liquidus isotherms with respect to TE at the onset of DS for # 11_6_17. Circles correspond to the thermocouple locations and * correspond to the locations of transverse section. The lines are the 4 th degree polynomial fit to the thermocouple measured profiles.	40
23. Mushy-zone freezing time verses distance for transverse sample locations (#11_6_17)	41
24. Mushy zone freezing rate with respect to distances of transverse samples (#11_6_17)	41
25. Growth speed with respect to distances of transverse samples (#11_6_17).....	43

26. The liquidus and eutectic thermal gradients with respect to distances of transverse samples (#11_6_17).	45
27. Temperature along the sample length with respect to time for #12_11_17 sample ..	46
28. Temperature variation from 290 C (C above the liquidus) to 250 C (C below the eutectic) as a function of time for sample #12_11_17	46
29. Distance of eutectic and liquidus isotherms with respect to TE at the onset of DS for #12_11_17. Circles correspond to the thermocouple locations and * correspond to the locations of transverse section. The lines are the 4 th degree polynomial fit to the thermocouple measured profiles.	47
30. Mushy-zone freezing time verses distance for transverse sample locations (#12_11_17)	48
31. Mushy zone cooling rate with respect to distance for 12_11_17.....	49
32. Growth speed with respect to distance of sample (#12_11_17)	51
33. Thermal gradient verses Distance on sample 12_11_17.....	52
34. Effect of furnace cooling rate on the mushy-zone freezing time at transverse sections located at increasing distance from TE at the onset of DS. (a) #11_6_17, (4 °C/min) (b) # 12_11_17, (0.5°C /min).	54
35. Heat extraction from the top of the ampoule region becomes more dominant as compared with that from the bottom cold end of the sample as liquid-solid interface moves towards the top and the liquid left is at relatively low temperatures.	55
36. Effect of furnace cooling rate on the eutectic and liquidus isotherm speeds as a function of distance from TE at the onset of DS (a) #11_6_17 (4 C/min) (b) # 12_11_17 (0.5 C/min).	55
37. Effect of furnace cooling rate on the eutectic and liquidus isotherm thermal gradient as a function of distance from TE at the onset of DS (a) #11_6_17 (4 C/min) (b) # 12_11_17 (0.5 C/min).	56
38. Fraction eutectic verses distance from eutectic	56
39. Longitudinal macrosegregation (C_s/C_o) as a function of fraction solidified (f_s).....	57
40. $\log (C_s/C_o)$ vs. $\log (1-f_s)$	58

41. Minimum spanning tree for #11_6_17 at various location from heat extraction end (a) 1 cm (b) 2 cm (c) 3 cm (d) 4 cm (e) 5 cm (f) 6 cm (g) 7 cm (h) 8 cm (i) 9 cm (j) 10 cm (k) 11 cm..... 60
42. Minimum spanning tree for #12_11_17 at various location from heat extraction end (a) 1.75 cm (b) 2.75 cm (c) 3.75 cm (d) 4.75 cm (e) 5.75 cm (f) 6.75 cm (g) 7.75 cm (h) 8.75 cm (i) 9.75 cm (j) 10.75 cm (k) 11.75 cm (l) 12.75 cm (m) 13.75 cm 61
43. Variation in Minimum Spanning Tree primary spacing with solidification distance. (a) 4 C/min cooling rate (sample #11_6_17) and 0.5 C/min cooling rate (sample#12_11_17). The dashed line is primary spacing predicted for Hunt-Lu [18] model for dendrite morphology and the dotted line is Hunt-Lu prediction for cell morphology. The distance at which cell to dendrite transition was observed is indicated by the red vertical line. 62
44. Variation in nearest neighbor primary spacing with solidification distance. (a) 4 C/min cooling rate (sample #11_6_17) and 0.5 C/min cooling rate (sample#12_11_17). The dashed line is Hunt-Lu [18] predictions for dendrite morphology and the dotted line is Hunt-Lu prediction for cell morphology. The distance at which cell to dendrite transition was observed is indicated by the red vertical line. 64
45. Ratio of the experimentally observed nearest neighbor primary spacing to that predicted from Hunt-LU model for dendrite morphology during DS..... 65
46. Variation in Primary Dendrite Trunk diameter as a function of solidification distance. (a) 4 C/min cooling rate sample# 11_6_17 (b) 0.5 C/min cooling rate sample #12_11_17. The dotted line is the trunk diameter predicted from analytical model [19] which is strictly valid only for the dendrite morphology and not for the cells.. 66

CHAPTER I

INTRODUCTION

1.1 Directional Solidification (DS) of alloys

Metal alloys are the combination of metal and metal or non-metallic element. Casting is a manufacturing process by which liquid metal poured into a mold is allowed to solidify. During directional solidification (DS) the heat is extracted from one end of the mold and the solid-liquid interface moves from one end of the casting to the other in a directional manner. The grains get aligned along one direction during DS, as opposed to the randomly oriented grains forming in the usual casting, aligned grains provide greater high temperature creep resistance along their longitudinal direction. This becomes especially useful for the gas turbine engine blade components in modern aerospace or land-based power turbines, as these rotating blades are the most stressed high temperature components in an engine [1].

During typical DS process a mushy zone forms between the bulk liquid which is yet to solidify and the portion that is already solidified. Fig. 1 shows a typical mushy-zone formed during DS of a transparent metal analogue alloy, succinonitrile-0.9% water. Here, the transparent phase is liquid, and the opaque tree-like phase is the primary

α solid. The trees, called primary dendrites, extend from their base at the alloy eutectic temperature to their tip at the liquidus temperature. The hot bulk melt is above the mushy zone and the cooler already solidified portion is below the mushy-zone. If a constant thermal gradient is maintained during directional solidification, then the mushy-zone length remains constant along the length of sample as is solidified from one end to the other. The last liquid to freeze in the inter-dendritic region at the tree-bottoms is of the eutectic composition (C_E), which when solidified results in a microstructure made of two finally distributed solid phase (α and β), often forming alternating plates of α and β .

For a constant thermal gradient, the liquid-solid interface is planar at very low growth speeds, it develops fingers of solid protruding solid phase (cells) at slightly higher growth speed. These fingers develop side-arms (called secondary branch) as the growth speed increases. At still higher growth speed higher order branches form (tertiary etc.) and the primary dendrite gains a well-branched tree like morphology [2]. Two important dendrite array morphology features, the primary dendrite spacing (λ) and the primary dendrite trunk diameter (TD) are also indicated in Figure-1.

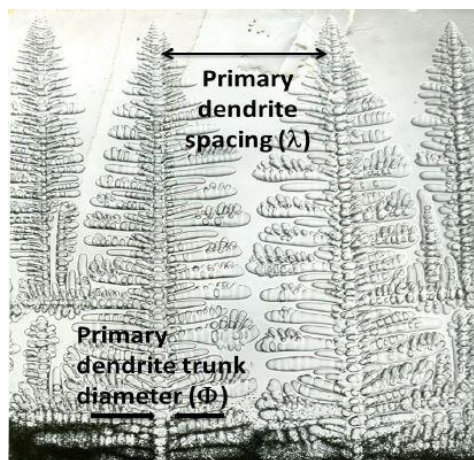
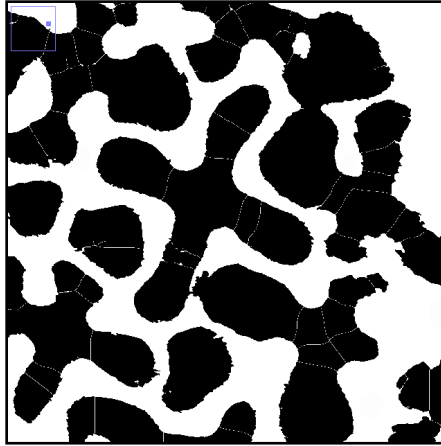


Figure 1. Succinonitrile – 9 wt. % Water “Transparent alloy” directionally solidified ($\sim 5\mu\text{m s}^{-1}$, $\sim 30\text{Kcm}^{-1}$) (Dr. Grugel, NASA-MSFC)

A typical transverse section of the primary dendrite array in DSed Pb-5.8Sb alloy is shown in Figure 2(a). The orthogonal nature of the branching is a consequence of (111) planes having the lowest liquid-solid interface free energy in face-centered cubic metals [3]. As explained above these side-arms develop their own braches as typically shown in the transverse view of one Pb-5.8Sb alloy primary dendrite in Figure 2(b).



(a)



(b)

Figure 1. Transverse view of, (a) Side Arms of Primary Dendrite in DSed Pb-5.8 Sb alloy and (b) Secondary, tertiary, and higher order branches in a typical DSed Pb-5.8 Sb alloy.

1.1.1. Directional Solidification Methods

Directional solidification can be carried out by two different procedures, “Steady State DS” and “Gradient Freeze DS”. For this research we selected the Gradient Freeze DS process.

1.1.1.1. Steady State DS

During steady-state DS the thermal gradient (G_L) and the growth speed (R) or both controlled independently and are maintained constant throughout the solidification process [4]. A DS furnace assembly typically consists of a hot-zone on top, and cold-zone at bottom, with an adiabatic zone in between. The furnace surrounds the ceramic crucible containing the alloy sample. The crucible is held stationary and DS is achieved by moving the furnace assembly from one end of the sample to the other. Since, in a given alloy the morphology and distribution of primary dendrite trees depend upon R and G_L , a constant dendritic microstructure forms along the entire length of the sample during steady-state DS. As shown schematically in Figure 4, three different growth speeds (typically three different DS experiments) would be required to obtain samples with three different dendrite morphologies using steady-state DS.

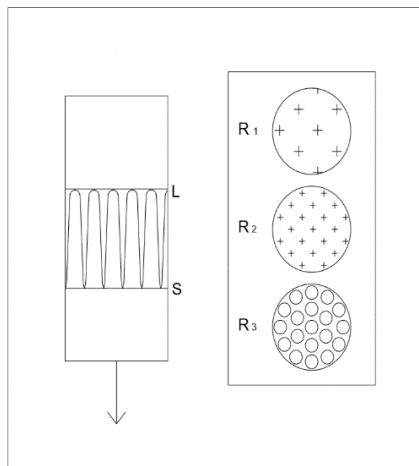


Figure 2. Schematic of steady state directional solidification

1.1.1.2. Gradient freeze directional solidification

During gradient freeze process the crucible containing the alloy sample and the hot-zone heating the mold are both held stationary [4]. The heat is extracted from one end of the crucible while the liquid-solid interface traverses from the cold end to the hot end. Here, independent control of R and G_1 is not possible. Only the rate at which the furnace is cooled can be controlled. Therefore, R (cm/s) and G_1 (K/cm) vary along the sample length, their variation itself depends upon the cooling rate (K/s). As a result, dendrite array morphology varies from one end of the casting to the other. The advantage, however, is that one sample can yield several dendrite morphologies along the DS length, depending upon the furnace cooling rate, as shown schematically in Figure 4.

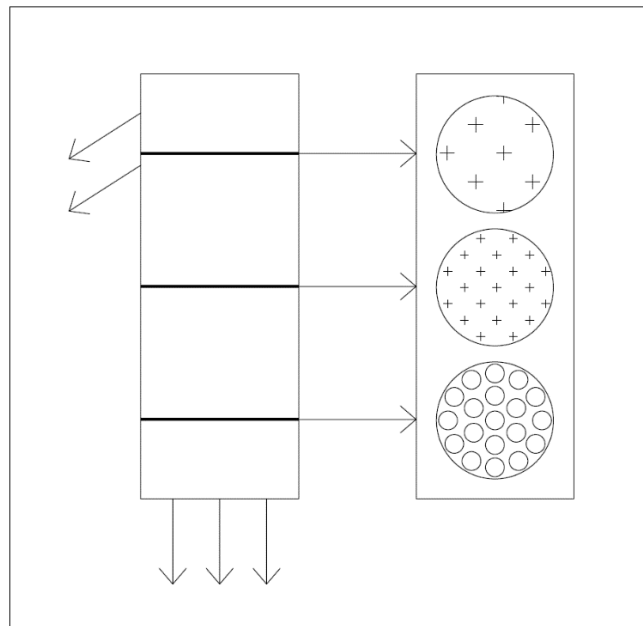


Figure 3. Schematic of gradient freeze directional solidification

1.2. Convection During Directional Solidification

1.2.1. Thermally and Solutally Stabilizing Growth

As explained above the temperature at the dendrite array tips, is approximately the liquidus temperature (T_L) of the alloy (the radius of curvature lowers the equilibrium

temperature by small amount) [5], and at the array bottom it is the eutectic temperature (T_E). With the gravity-vector pointing downwards (as on earth), the temperature effect alone is stabilizing against natural convection because the increasing melt temperature decreases the melt density. However, the solutal concentration profile depends upon the composition dependence of the interdendritic melt for the alloy being directionally solidified [5]. Let us recall that for alloys with solute partitioning coefficient (k) less than unity, the melt composition in the interdendritic melt varies from solute rich eutectic (C_E) at the bottom of the array to the solute poor composition (C_t) liquid at the array tips. C_t is actually slightly higher than the alloy composition (C_o) because of the curvature effect [5]. If the alloy is such that increasing solute content increases its melt density, then the composition profile in the interdendritic melt is also stabilizing against natural convection [6]. This is the case for example with the Al-19 wt% Cu alloy because increasing copper content of an aluminum-copper alloy melt increases its density (as shown schematically in Figure 5).

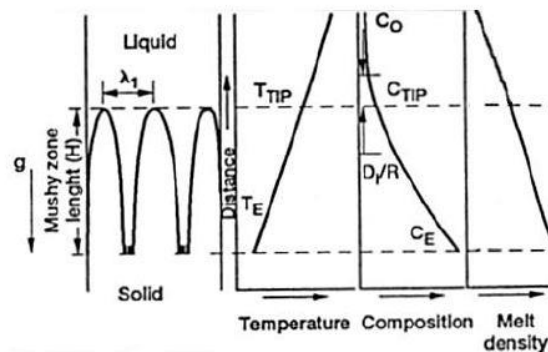


Figure 4. Schematic Temperature, Concentration and Density Profiles in inter-dendritic Liquid, Al-Cu

1.2.2. Thermally Stabilizing, but Solutally Destabilizing Growth

However, if the alloy is such that the increasing solute content decreases its melt-density, then a density inversion occurs in the inter-dendritic melt and the DS process is

potentially susceptible [7] to natural convection, as shown schematically in Figure 6. This is the case with Pb-5.8 Sb [8]; the increasing Sb content of a Pb-Sb alloy melt decreases its density.

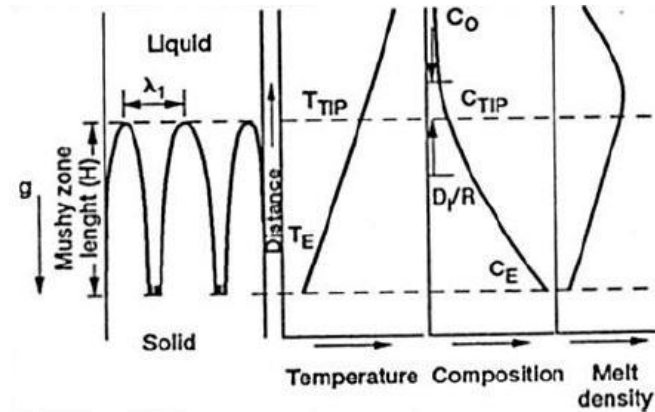
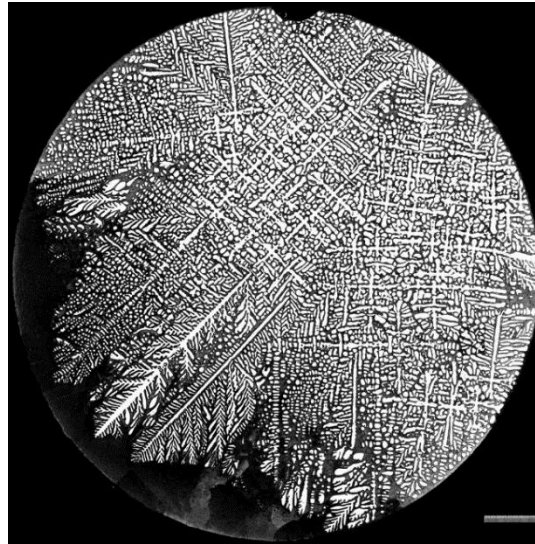


Figure 5. Schematic Temperature, Concentration and Density Profiles in inter-dendritic Liquid, Pb-Sb⁸

1.3. Convection and Dendrite Array Morphology

Natural convection occurring in the mushy zone alters the local thermal and solutal profiles and hence it influences the dendrite array morphology and their uniformity across the cross section of the Directional solidified product. Even in situations where thermal and solutal profiles are expected to be stabilizing against natural convection, presence of radial temperature gradient causes some primary dendrites to lag their neighbor. When that happens the solute rich melt ahead of the leading dendrite begins to flow downwards retarding the growth of lagging neighbors even more. This makes the leading edge of the dendrite array “steepled” and can lead to severe radial macrosegregation, as for example shown in Fig. 7 for an Al-19%Cu alloy [9]. The central region where the leading dendrites existed has more primary dendrite trees, but going radially outwards the dendrites are very non-uniform. Some of them have unusually long side-arms on their

one side. There almost no dendrites in the very outer region, where the microstructure is entirely eutectic.



(b)

Figure 6. Image of transverse slice of an Al-19 % Cu alloy, grown at $10 \mu\text{m s}^{-1}$. This depicts an example of transverse phase macrosegregation.

In alloys, such as, Pb-5.8% Sb where the interdendritic region is solutally stabilizing, the low density solute rich melt begins to flow upwards creating “plume type” convection, because density of Pb is 11.34 and that of Sb is 6.64 g cm^{-3} . The “plume convection” produces an Sb macrosegregation along the DS length of the samples [10], and is known to reduce the primary dendrite spacings as compared with theoretical predictions [11]. When the neighboring plumes combine together they can create even severe defect, called, freckles or channel segregates in the microstructure, as shown in Fig. 8 for a Pb-5.8 wt% Sb alloy. These are the regions where the solute rich melt flowing upwards causes re-melting of already solidified side branches of the primary dendrites leaving fragmented branch pieces along its path.

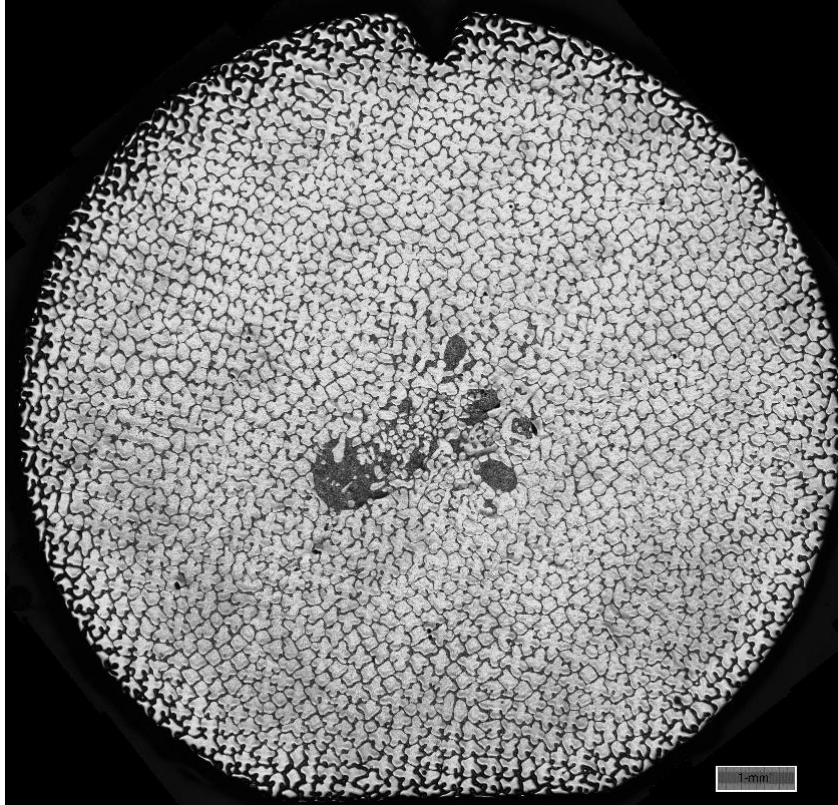


Figure 7. Image of transverse slice of a Pb-6 % Sb alloy. This depicts an example of channel formation because of plume type thermos-solutal convection.

1.4. Theoretical Models to Describe Primary Dendrite Morphology

Because of the numerical complexities to account for mass transfer and phase equilibrium existing at the solid liquid interface at length scales which are in micrometers, the array dimensions which are in millimeters, and the ampoule dimensions where heat-transfer and fluid flows are occurring being in several centimeters, and the interdependence of the array morphology, permeability, and convection, it has not been possible so far to generate an accurate three dimensional numerical model which can predict the effect of convection on the dendrite array morphology. Therefore, the theoretical models to predict array morphology features, such as, dendrite tip radius, the primary spacing, and dendrite trunk diameter all assume pure diffusive transport and

completely ignore the convection effects [12-15]. Effect of convection has only been modeled as empirical parameter fit to the experimental data based on very simplistic assumptions [16-17]. Two typical diffusive models which predict the primary dendrite spacing [18], and the primary dendrite trunk diameter [19] are described below.

1.4.1. Primary Dendrite Nearest Neighbor Spacing Hunt-Lu [18] Model

This semi-theoretical model predicts dendrite tip radius (ρ), primary dendrite spacing (λ) and dendrite tip composition (C_{tip}). This semi-empirical Hunt-Lu model used experimental polynomial ‘fit’ parameters and has proven to correlate the microstructure observed in a broad range of thermal gradient, growth speed and compositions. For primary spacing, this will be the only model used here to compare the experimental results. This model uses several dimensionless parameters:

$$G' = \frac{G\Gamma}{(mC_o)^2}$$

$$V' = \frac{V\Gamma}{DmC_o}$$

$$\lambda' = \frac{\lambda m C_o}{\Gamma}$$

Where, $\Delta T_o = \frac{m_i C_o (k-1)}{k}$, G = effective thermal gradient, Γ = capillary length (proportional to the ratio of solid-fluid surface energy to the heat of fusion), D = diffusion coefficient of Sb in melt, k = solute partition coefficient, C_o = initial alloy composition, mL = liquidus slope, and λ = Primary dendrite spacing.

For calculation, all variables are assumed to be constant. The HL model predictions with the above parameters are given as:

- Curvature Undercooling $\Delta T'_\sigma$

$$\Delta T'_\sigma = 0.41(V' - G')^{0.51}$$

- Tip radius ρ

$$\rho = \frac{2\Gamma}{\Delta T'_\sigma \Delta T_0}$$

- Primary spacing λ'

$$\lambda' = 0.15596V'^{(a-0.75)}(V' - G')^{0.75}G'^{-0.6028}$$

$$a = -1.131 - 0.1555 \log(G') - 0.007589[\log(G')]^2$$

1.4.2. Primary Dendrite Trunk Diameter Model

This model developed by Tewari et. al [19] uses the dendrite tip radius predictions from the Hunt-Lu model, makes assumptions about the relationship between the tip radius and the initial trunk diameter (Φ_0) at the bottom of the paraboloidal shaped tip region (till just before the onset of side-branching), and then uses side-branch coarsening predicts the diameter of the dendrite tree at its bottom (Φ).

$$\Phi^3 = 96 \frac{D_l \Gamma}{VG(1-k)} \ln \left\{ \frac{1 + \frac{VGt}{m_l C_0}}{1 + \frac{VGt_0}{m_l C_0}} \right\} + \Phi_0^3$$

Where Φ_0 =initial trunk diameter with r_t being the dendrite tip radius, D_l = solute diffusion coefficient in the liquid, V = growth speed, G = thermal gradient, Γ = Gibbs-Thompson coefficient, k = solute partition coefficient, m_l = liquidus slope and C_0 = the alloy composition.

CHAPTER II

PURPOSE OF THIS RESEARCH

The driving reason for this research was the limitations of the equipment available on the International Space Station to carry out directional solidification of metallic alloys in the low gravity environment of space to compare predictions from the theoretical dendrite morphology models with experiments carried out under truly diffusive transport conditions. The primary European Space Agency owned facility (LGF) which was designed for this purpose is no longer available for future experiments. The question we had was, can we achieve the same scientific goals in a much simpler Gradient Freeze type of experimental facility which may become available on the Space Station in near future. Thus tis research had following goals;

1. Modify/Fabricate a gradient freeze DS furnace facility which can be used for low-melting point metal alloys.
2. Select an alloy suitable for such a study and demonstrate its feasibility by terrestrial experiments.

3. Demonstrate feasibility of generating cellular, cell to dendrite transition, side-branched dendrites and well-branched dendrites having tertiary and higher order branches in one DSed sample.
4. Investigate experimental parameters, such as, furnace hot-zone temperature, alloy composition, cooling rates, thermal profiles, etc. which clearly demonstrate natural convection effects on the dendrite array morphology during directional solidification.

CHAPTER III

EXPERIMENTAL AND ANALYTICAL PROCEDURES

1.1. Alloy selection

The phase diagram of Pb-Sb alloy system [20] selected for this study is shown in Figure 9. This alloy system was selected for this study, because, it has been extensively investigated by steady-state directional procedure in our laboratory in the past. Specifically Pb-5.8 wt% Sb alloy has a low liquidus temperature (288.1 °C), therefore will need low relatively less power to heat, melt, and provide adequate superheat for gradient freeze DS. Metallographic sample preparation techniques and the equipment required for its microstructural characterization are known and available. Thermal gradient and growth speed dependence of its primary dendrite spacing have already been extensively measured [8,10,11]. The physical properties required to predict the processing parameter dependence of primary spacing and dendrite trunk diameter are already known for this alloy system (Table-1). It has been shown in prior steady-state DS studies that it is prone to the interdendritic “plume” type convection [10].

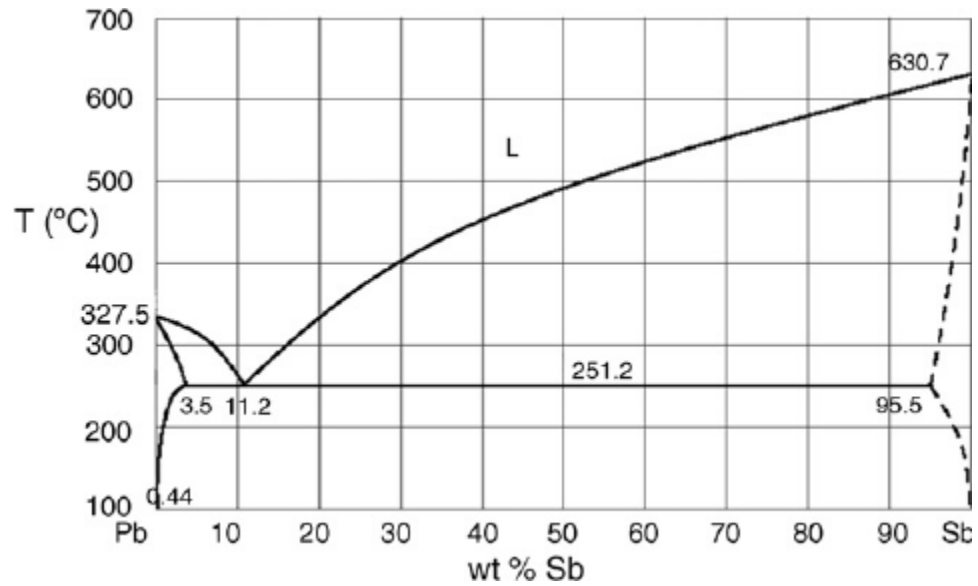


Figure 8. Pb-Sb Phase Diagram [20]

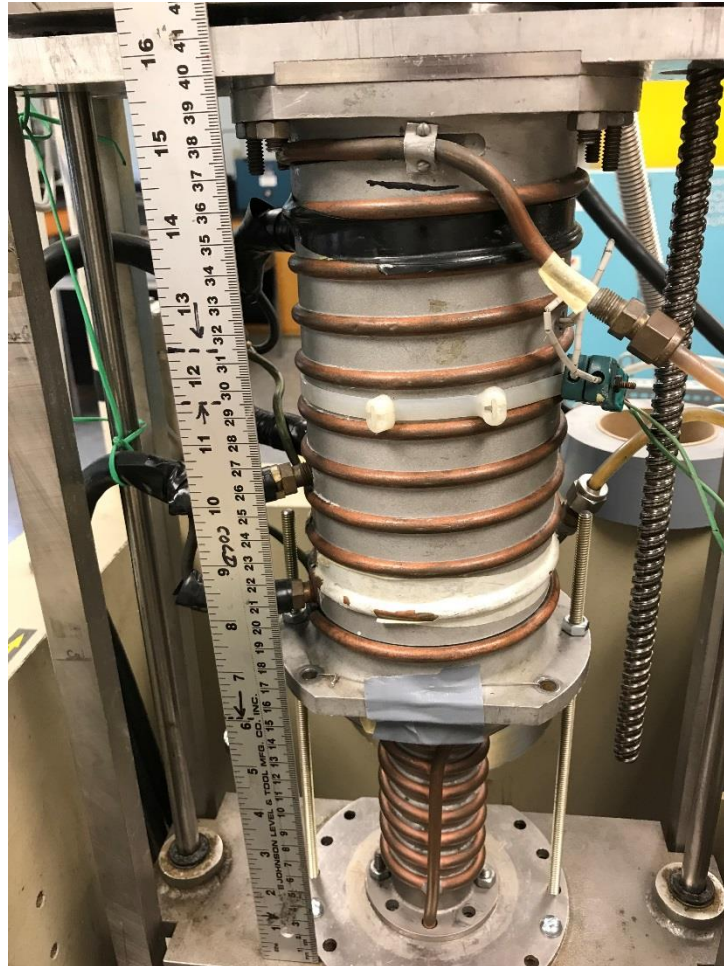
Name	Variable	Units	Value
Liquidus Temperature	T_L	C	288.1
Liquidus Slope	m_L	K/wt%	-6.78
Solute Partition Coefficient	k	Dimensionless	0.31
Eutectic Temperature	T_E	C	252.5
Heat of Fusion	Δh_f	Jm^{-3}	2.79×10^8
Eutectic Composition	C_E	wt%	11.2
Diffusion coefficient of Sb	D_L	cm^2/s	5×10^{-5}
Gibbs-Thomson Coefficient	Γ	μmK	0.12

Table 1 Thermophysical properties of Pb–5.8 wt. pct. Sb used to calculate predict primary dendrite spacing and trunk diameter.

1.2. Gradient Freeze DS Equipment and Procedure

Figure 10 shows the gradient freeze DS facility that was especially fabricated/assembled for this research. It consists of a hot-zone (larger diameter feature in Figure 10(a)) placed above the heat extracting liquid bath (smaller diameter feature in Figure 10(a)) below. The resistance heated hot zone is made of two ring heaters which can be independently controlled. The heat extraction bath is a cylindrical water cooled vessel containing molten gallium, a detailed view of this is presented in (Fig. 10(b)). A ceramic alumina disk having a circular hole separates the heated portion of the cylindrical quartz ampoule containing the Pb-5.8Sb alloy sample above from the heat extracting gallium bath below. The cylindrical quartz ampoule containing the sample is vacuum sealed at the bottom and is evacuated from the top by using a diffusion vacuum pump, giving typically ~10 millitorr of dynamic vacuum. Figure 10(c) shows one of the quartz ampoules containing the Pb-Sb sample used in this research. Ten fine tipped chromel-allumel thermocouples are attached to the ampoule outer surface at separation distances of 1 to 1.5 cm to record the temperature along the length of the sample as a function of time using a data-logging system. Location of the thermocouples is indicated in Figure 10(c). A [100] oriented Pb-5.8Sb seed rod is kept at the bottom with additional remelt stock above. The furnace is slowly heated first to the set super heat temperature, it is held at that temperature for about 45-minutes, and then allowed to cool at a controlled cooling rate. As a result the feed bar above melts and fuses to the [100] oriented seed below before being re-solidified in a directional manner because of the heat being extracted from the bottom end. After several attempts optimum hot-zone temperature and cooling rates were established. With a hot-zone temperature of 650 C two samples were finally

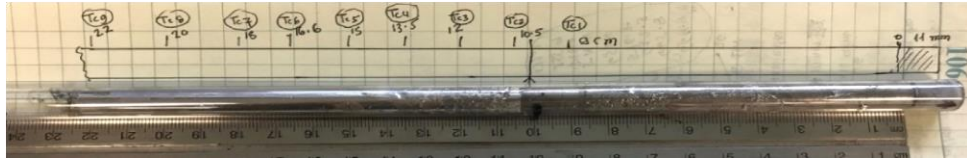
directionally solidified at slow and fast cooling rates, 0.5 C/min and 4 C/min, as listed in Table-2 below.



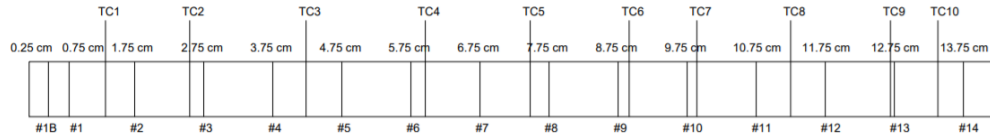
(a)



(b)



(c)



(d)

Figure 9. Gradient Freeze DS facility and process. (a) Gradient Zone DS facility (b) Detailed image of the heat extracting gallium bath at the bottom, (c) typical quartz crucible in this research showing the locations where chromel-alumel thermocouples were attached on its outer surface, (d) Locations of the thermocouple tips as a function of distance from the initial location of T_E at the onset of DS.

Sample ID	Sample Dimension	Cooling Speed
Pb-Sb-12_11_17	Constant 9 mm	0.5 °C/min
Pb-Sb-11_6_17	Constant 9 mm	4 °C/min

Table 2 Growth conditions of two Pb–5.8 Sb samples examined in this study.

1.3. Specimen preparation (transverse sections) and metallography

The experimentally obtained thermal profile during the DS process (typically shown in Figure 12 for a sample cooled at 4 C/min) was used to obtain the initial location of the Eutectic Isotherm (T_E) at the onset of directional solidification. Then transverse sections were cut along the sample length at 0.5, 1, and 1.5 cm distances with respect to the TE for further metallograohy and image analysis. Typical transverse section locations and their corresponding IDs were also shown in Figure 11 shown above.

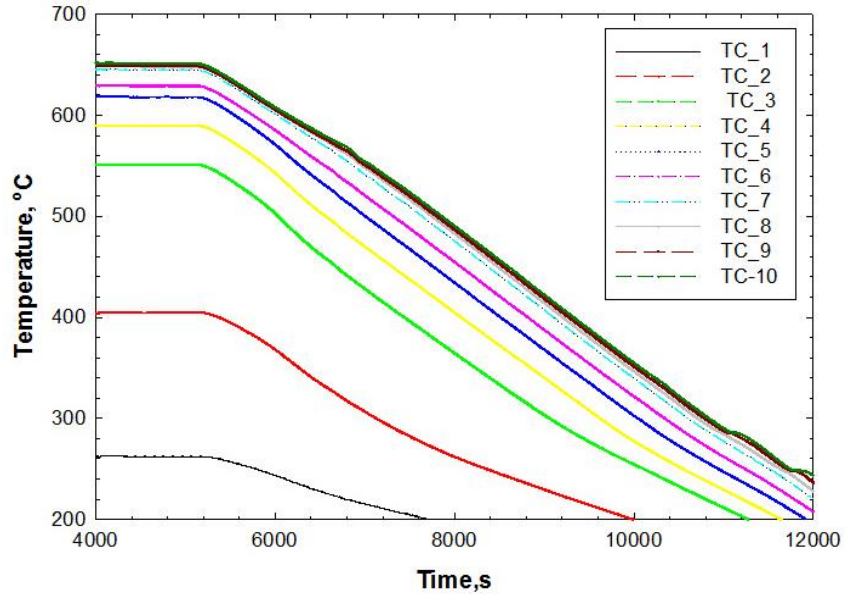


Figure 10. Temperature profile recorded by ten thermocouples located at known separation distances as a function of processing time for a typical gradient-freeze DS at a 4 C/min furnace cooling rate.

1.3.1. Cutting, Mounting, And Polishing

A thin groove was machined all along the sample length of the Directional solidified sample prior to cutting transverse slices off so that transverse images taken at various distances can later on be aligned with respect to each other. A low-speed, variable RPM, precision wafer saw was used to cut the samples at various pre-determined locations by using diamond tipped low-grit precision saw blades having 0.3 mm thickness. Once sliced, the “hot end” of each slice was marked by black ink for their further mounting. The cut slices were cold mounted. A cylindrical plastic mold was lubricated with industrial oil and the specimen was placed in the middle of the mold with the “hot side” facing downward. In a separate container, 30 mL of Struers Epofix resin was carefully mixed with 15 mL of Struers Epofix hardener to create an epoxy mixture. The epoxy mixture was then poured over the cylindrical mold and allowed to cure overnight.

A Leica SM2500E Ultramiller was then used to further prepare the surface of the mounted sample for subsequent polishing. The surface preparation procedure consisted of two steps: the initial machining using a pre-miller, followed by final machining using suitable diamond blades to obtain a mirror-like surface. Ethylene glycol was used as a lubricant during ultramilling process. The adhered residue materials on the sample surface were then removed by using a water ultrasonic bath. A 9 mm Buehler Chemomet polishing cloth was used for final polishing step. Chemomet cloths are soft, porous, chemical-resistant, synthetic pad for softer materials which works well with the Pb-Sb surface. The polishing conditions used in this research are presented in Table 3.

Average Grade (Grit)	Force	Time (min)	Polishing Pad RPM
9 mm Chemomet	21 lbs	7	110
9 mm Chemomet	21 lbs	7	110 (opposite rotational direction)

Table 3 Polishing procedure for 9-mm to 12.7-mm diameter sections sample preparation

To eliminate contamination during polishing, 0.05 μm alumina slurry suspension was generously added on the surface of the polishing cloth. It is imperative to thoroughly clean the polishing cloth and specimens under running water after each round of polishing to eliminate alumina residue. Samples often need to be re-polished, solvated with ethyl alcohol, or cleaned in an ultrasonic bath to remove remaining colloidal alumina particles and oil. Avoid over-polishing as this can lead to wearing away of the softer alpha phase, creating an embossed surface with beveled edges on the final image that will be captured. Once finished, each sample was dried and then observed under the microscope for image capturing.

1.3.2. Optical Microscopy

A metallurgical brightfield inverted Nikon microscope with an attached 5.0-megapixel digital camera utilizing SPOT 5.0 Image software was used to capture magnified images of the sample's surface (50X). For such a large field of view, several overlapping images had to be taken by manually translating the microscope stage. A 12.7 mm (1/2 in) diameter cross-sections sample typically required upwards of 90 images to cover the entire cross-section. The original digital images were saved with .TIF extensions for subsequent image-stitching using Photo Shop software. Parameters such as light exposure, gamma corrections, gain, and color-filters were manually selected to create best image quality and varied from sample-to-sample. Ideal image quality was seen to possess constant light intensity across the whole field of view, for one phase and between samples and images. High contrast light absorption differences between lead and antimony also aids in distinguishing phases that were present. It was important to clean and align the microscope's projection lenses to capture consistent images. Typical settings include: 140 ms of exposure, a 1.00 gain factor, gamma correction of 0.50, and a green-tint light filter. For each sample, a known 1-mm scale was imaged to record pixel to millimeter ratio for images. But, oxide layers were known to grow rapidly on the metal's surface if samples were stored for later microscopy. This is often avoided to eliminate unevenness in the overall quality of the image.

1.3.3. Montage Making and Image Analysis

Adobe Photoshop CS5.1 on 64-bit Windows 7 on an HP z210 workstation was used for image stitching and montage making to obtain the high resolution image of the entire sample cross-section for subsequent morphological analysis. Image stitching is the

process of multiple photographic images with overlapping fields of view to produce a segmented high-resolution image. To adjust distortions, transformations for microscopic images are not required. Image stitching is simplifying the “Image registration” of locations or the process of transforming different sets of data into one coordinate system. Difficulties in conducting image stitching stems from intensity differences between images, intensity gradient in an image and partial unfocused features. Averaging intensities and colors can blend two images to hide seams. Larger digital files are more difficult to stitch because they require more computing capabilities. For the larger cross-section area slices like 120, image stitch required 10-14 hours of computing time and often lead to computer ‘freeze’. For smaller cross-sectional area like 10-20, smaller image collection needs 10-15 minutes to stitch.

The montaged images were then suitably rotated using the surface groove machined along the sample length, such that the groove in each of the image was located at 90 deg.

ImageJ v. 1.46 was used to measure primary dendrite trunk diameter. ImageJ is an open source National Institute of Health image analysis program that can be downloaded from <http://rsb.info.nih.gov/ij/> for a variety of operating systems. Drawing a line between two pixels with (x,y) coordinates can calculate length $d = \sqrt{x^2 + y^2}$. Appropriate measurement values must be selected prior to drawing line segments. This is done by choosing Analyze > Set Measurements > Bounding rectangle > OK, which measures a rectangle bounded by the two end points of the line segment acting as a diagonal. After choosing the line-selection tool and making a line-selection on an image, choosing Analyze > Measure will print a set of numbers for a ‘Bounding rectangle.’

A bounding rectangle has 6 measurements labeled BX, BY, Width, Height, Angle, and Length. A rectangle can be drawn with the extreme values of x and y for the four corners of the rectangle provided a line segment with two sets of (x,y) coordinates. The line drawn is arbitrarily set as one of the diagonals. 'BX' and 'BY' are the upper-left x and y coordinate in pixels in relation to the upper-left corner of an image, 'Width' and 'Height' are the width and height of the bounding rectangle, 'Angle' is the minimum angle between the drawn line and an imaginary line facing due right from the 'starting' point for the drawn line, and 'Length' is the length of the drawn line.

1.3.4. Dendrite Trunk Diameter

For the dendrite trunk diameter measurement, two lines are drawn such that each line is a minimum distance spanning the trunk, as shown in Figure 12. For an ideal well-formed dendrite, these two lines will be perpendicular to each other. The diameter of that trunk was taken as the average of those two lines lengths in pixels. Dendrite center was also calculated from these measurements by knowing the intersection of these two lines. This calculation was done through a computer program written in VBA coding language for Excel 2010, listed in the appendix. Though dendrite center absolute (x,y) coordinates are irrelevant, coordinates are important for spacing calculations which will be discussed in the later sections.

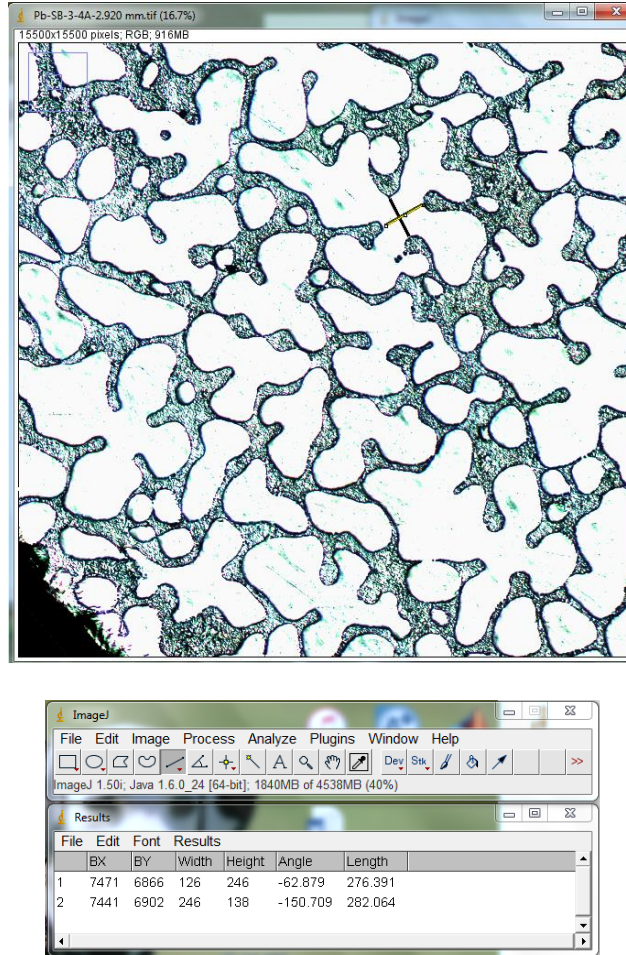


Figure 11. Screen capture of bounding rectangle measurement for trunk diameter

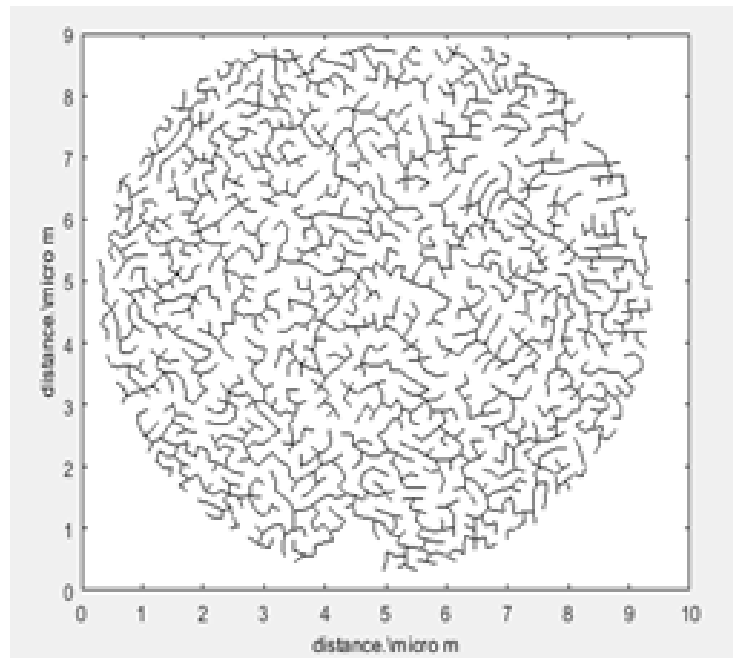
1.3.5. Primary Dendrite Spacing

1.3.5.1. Nearest Neighbor Spacing

Numerical analysis using dendrite center (x,y) coordinates measured in ImageJ allows for the calculation of nearest neighbor spacing. The minimum of the set of all possible distances were calculated with a caveat that the set of all possible distances will not contain duplicates through the symmetric property of equality. Given a set of (x,y) coordinates, a VBA macro code for Excel 2010 was written to calculate nearest neighbor spacing.

1.3.5.2. Minimum Spanning Tree

A minimum spanning tree is obtained by connecting all the center of mass values which are obtained from the image analysis (Typically shown in Figure13). It represents the shortest total distance by connecting all the nodes, without having any closed loop. The center which is nearest to the other dendrite is located and joined to form network and this process is repeated until all the centers of dendrites are connected to the minimum spanning tree. Mean and standard deviation values of the branch lengths are also used as representing the primary dendrite spacing.



12. Minimum Spanning Tree for a directionally solidified Pb-5.8 Sb alloy microstructure.

1.3.6. Fraction Eutectic

1.3.6.1. Thresholding

The composition at a location can be calculated if the fraction eutectic is known. Fraction eutectic can be calculated using the area covered by the eutectic region divided by the total area of the sample. The difference in color intensities of the lead-rich and

antimony-rich region based on their light absorption allows for identification of distinct structures from captured images. High intensity lead-rich α phase can then be separated from the antimony-rich eutectic. Thresholding allows for the separation of pixels based on intensity values (Figure 14). For 8-bit image pixels are labeled between 0 and 255 based on intensity where black is assigned a value of 0 and white is 255. A number is chosen where all numbers equaling that value or higher will be given a value of 255 and all lower a value of 0. Thresholding transforms an 8-bit grayscale image into a binary image of black and white pixels. Picking a proper cut-off intensity value is vital for accuracy to ensure user bias is not introduced as image intensity vary from sample to sample. ImageJ has a built-in thresholding algorithm under “default” which was used for thresholding.

A “Region of Interest” must always be selected before thresholding to eliminate unwanted background pixels that will not be included in the later calculation. In the ImageJ menu select: Edit > Selection > “Create Selection.” To execute the algorithm, select: Image > Adjust > “Threshold.” The image can be inverted so that the dendrite phase is black, and the antimony-rich phase is white. In the case where the values for black and white are inverted select: Image > Lookup Tables > “Invert LUT”. Hover over the black and white regions to ensure that the assigned values correspond to the correct color.

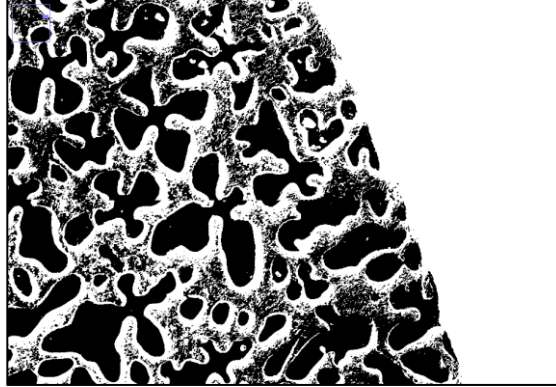


Figure 13. Typical example depicting the thresholding procedure of an 8-bit image of an Pb-Sb transverse slice with corresponding intensity histograms.

1.3.6.2. Watershed

The eutectic phase is composed of both antimony-rich (white region) and lead-rich phase (black regions within eutectic). Since not all black pixels can be considered a fraction of the dendrites as seen from Figure 15, the lead-rich metastable phases remaining within the eutectic which are colored similarly to the α phase should be separated and eliminated prior to fraction eutectic calculation. A watershed algorithm was used to accomplish this.

A watershed transformation draws 1-pixel wide white pixels through geographical minimum distances between regions of white. The binary image of antimony-rich white particles embedded into lead-rich black landscape are connected by a spider web of lines, sectioning the lead-rich black landscape into particles. It should be noted that the drawn white pixels add to the white count and subtract from the black count by 0.5 - 1% of the total pixel count (which can be calculated by [black particle count before watershed] - [black particle count after watershed]).



Figure 14. Typical example depicting the watershed and particle area cut-off procedure of a binary image.

1.3.6.3. Particle Size Cut-Off

After water shedding the image, individual particles are created from the previously connected lead-rich black regions within the eutectic. To eliminate eutectic α phase from being included in the calculation of primary dendrite α phase, particles having areas smaller than a specified pixel area cutoff value were ignored while measuring the area fraction occupied by primary dendrites. Pixel area cutoff value ranges from 1000-2500 pixels and may vary from image to image. Different cutoff values will affect results by 1-2% for 100% increase or decrease in area cut-off. Once this value is determined, the eutectic α phase particles can be selected as a “Region of Interest” and are then filled with white to eliminate its fraction contribution.

1.3.6.4. Fraction Eutectic Calculation

Fraction eutectic can be calculated once the eutectic black particles (eutectic α) are eliminated and a binary image has been created. Given a ‘Region of Interest’, the mean intensity value can be calculated. Particle’s values are 255 for white or 0 for black.

Therefore, $[\text{mean intensity}]/255 = [\text{fraction alpha}]$ and $1 - [\text{fraction dendrite}] = [\text{fraction eutectic}]$. As this process is standard from image to image, a macro was written for ImageJ to process a batch of images.

CHAPTER IV

RESULTS AND DISCUSSION

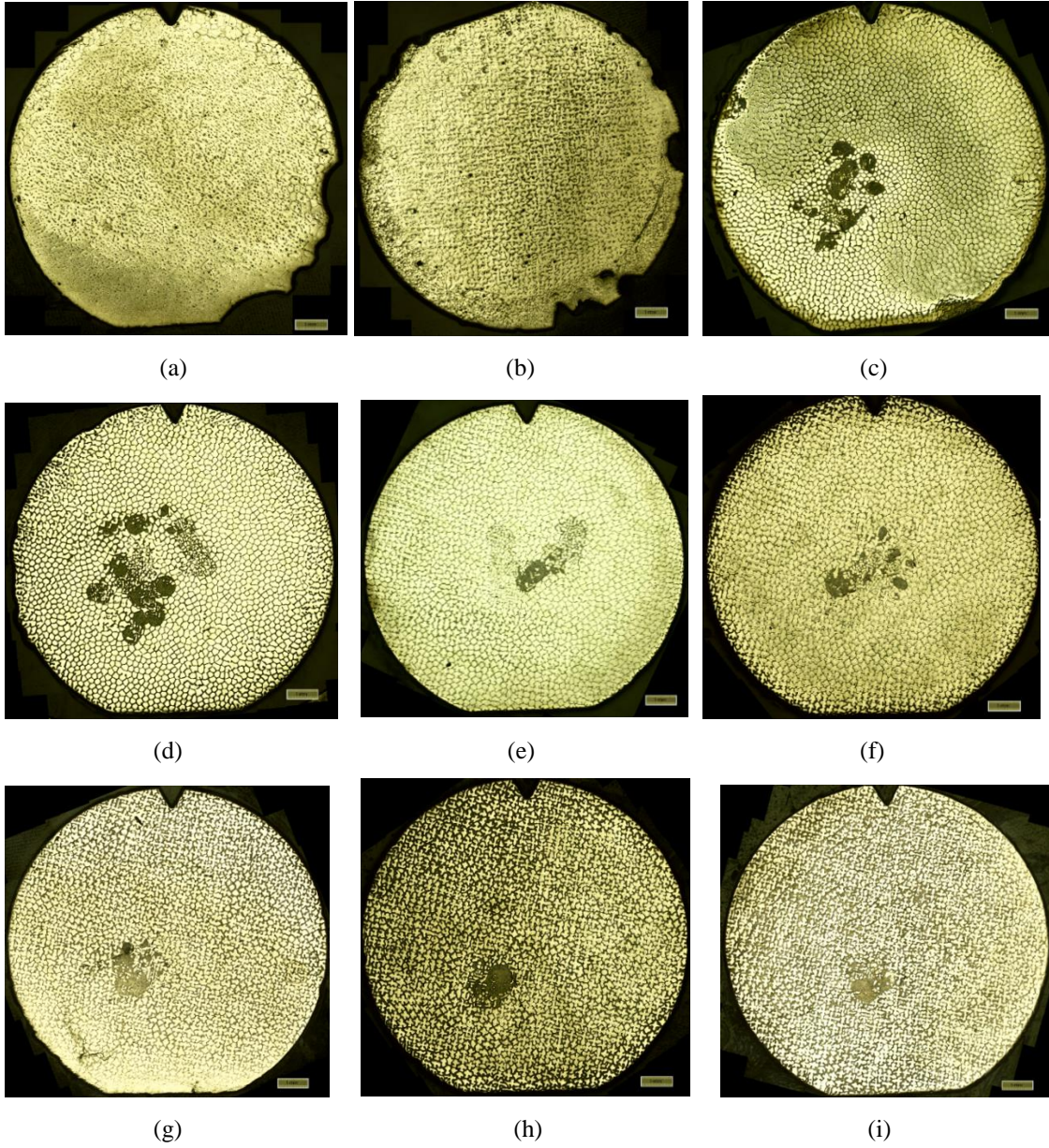
4.1. Dendrite Morphology Variations During Gradient Freeze DS

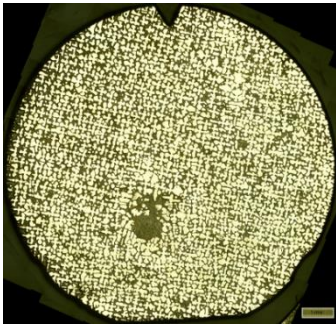
Transverse views along the directionally solidified length for the two samples examined in this research 12_11_17 and 11_6_17 with cooling zone 0.5°C and 4°C are presented below in Figures 16, 17, 18 and 19 below. The corresponding ID and distance with respect to the TE at the onset of DS for each section are listed in the figures.

4.1.1. Gradient Freeze DS at Slow Cooling Rate

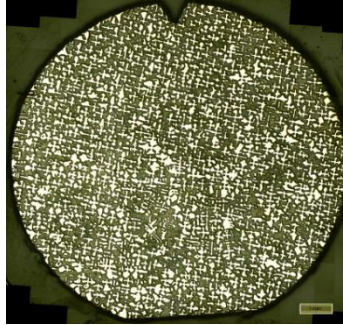
Figure 16 shows the transverse microstructures obtained from sample #12_11_17 which was solidified at 0.5 C/min cooling rate. Figure 17 shows higher magnification views from these sections. The dark interdendritic eutectic regions separate the primary dendrites. The morphology is initially cellular having no branches (Fig. 16 (b), (c), 17 (b), (c)). It shows cell to dendrite transition at approximately 2.75 cm (Fig. 16 (d) and Fig. 17 (d)) and formation of side-arms beginning at approximately 4.75 cm (Fig. 16 (f) and Fig 17 (f)). Well-branched dendrite arrays are obtained at a distance of about 5.75 cm (Fig. 16 (g) and Fig 17 (g)). These microstructures also suggest that the area fraction occupied by the eutectic portion is increasing as a function of solidification distance,

indicating a longitudinal segregation of Sb. This growth condition is susceptible to severe plume convection as seen by the channel segregates present on several transverse sections, especially during initial DS process.

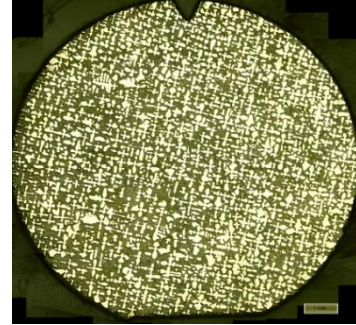




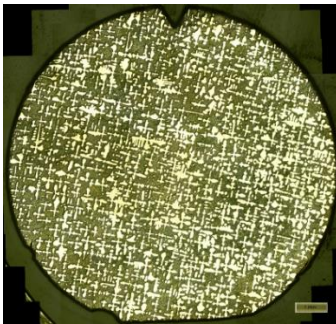
(j)



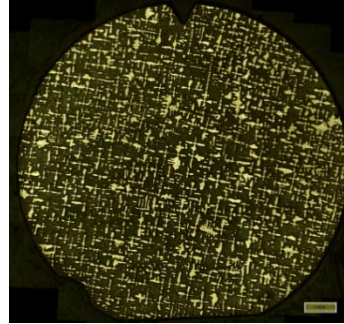
(k)



(l)

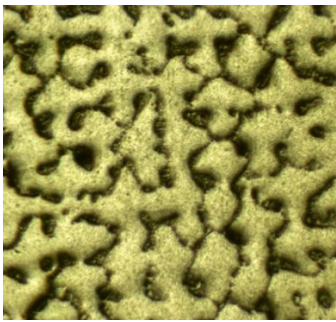


(m)

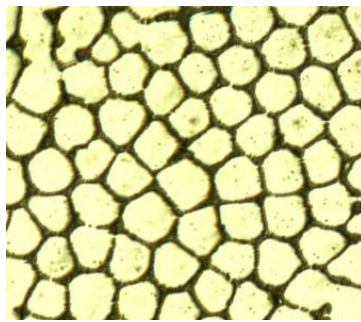


(n)

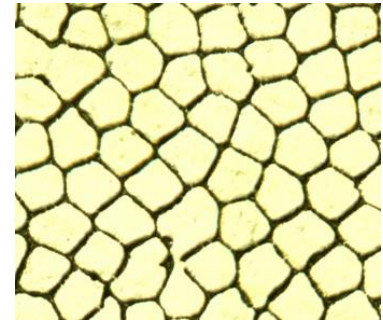
15. Transverse microstructure of 12_11_17 at different distance away from Te (a) 0.25 cm (b) 0.75 cm (c) 1.75 cm (d) 2.75 cm (e) 3.75 cm (f) 4.75 cm (g) 5.75 cm (h) 6.75 cm (i) 7.75 cm (j) 8.75 cm (k) 9.75 cm (l) 10.75 cm (m) 11.75 cm (n) 12.75 cm (o) 13.75 cm



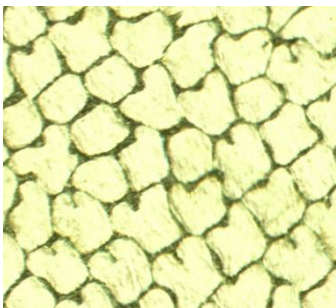
(a)



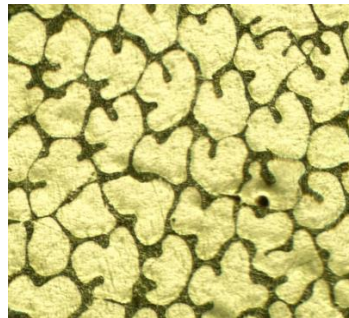
(b)



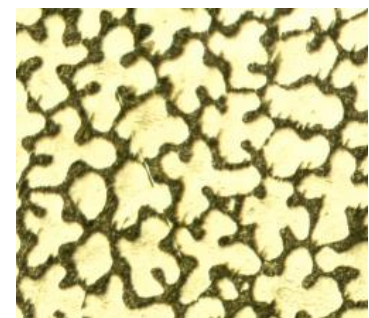
(c)



(d)



(e)



(f)

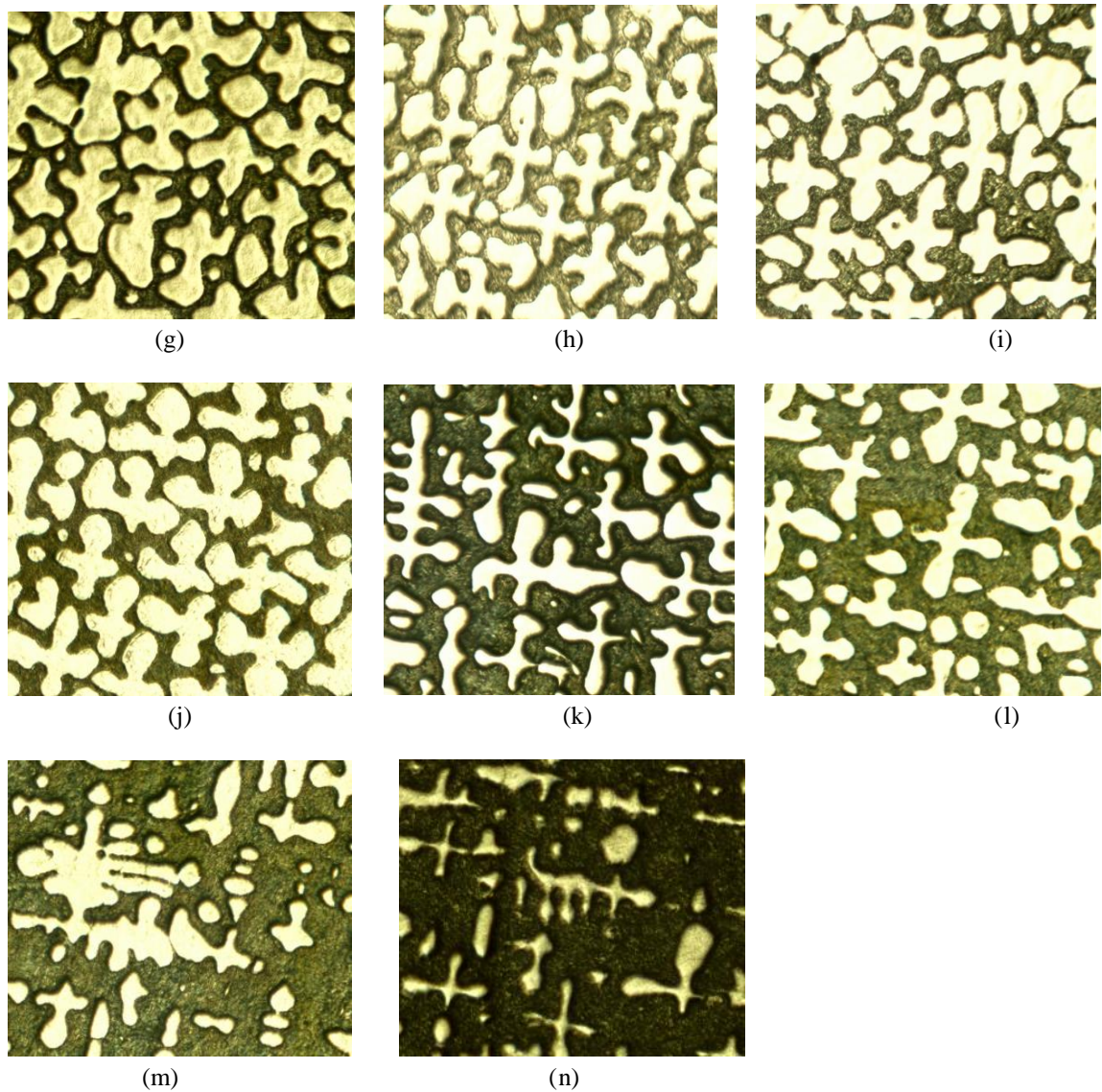
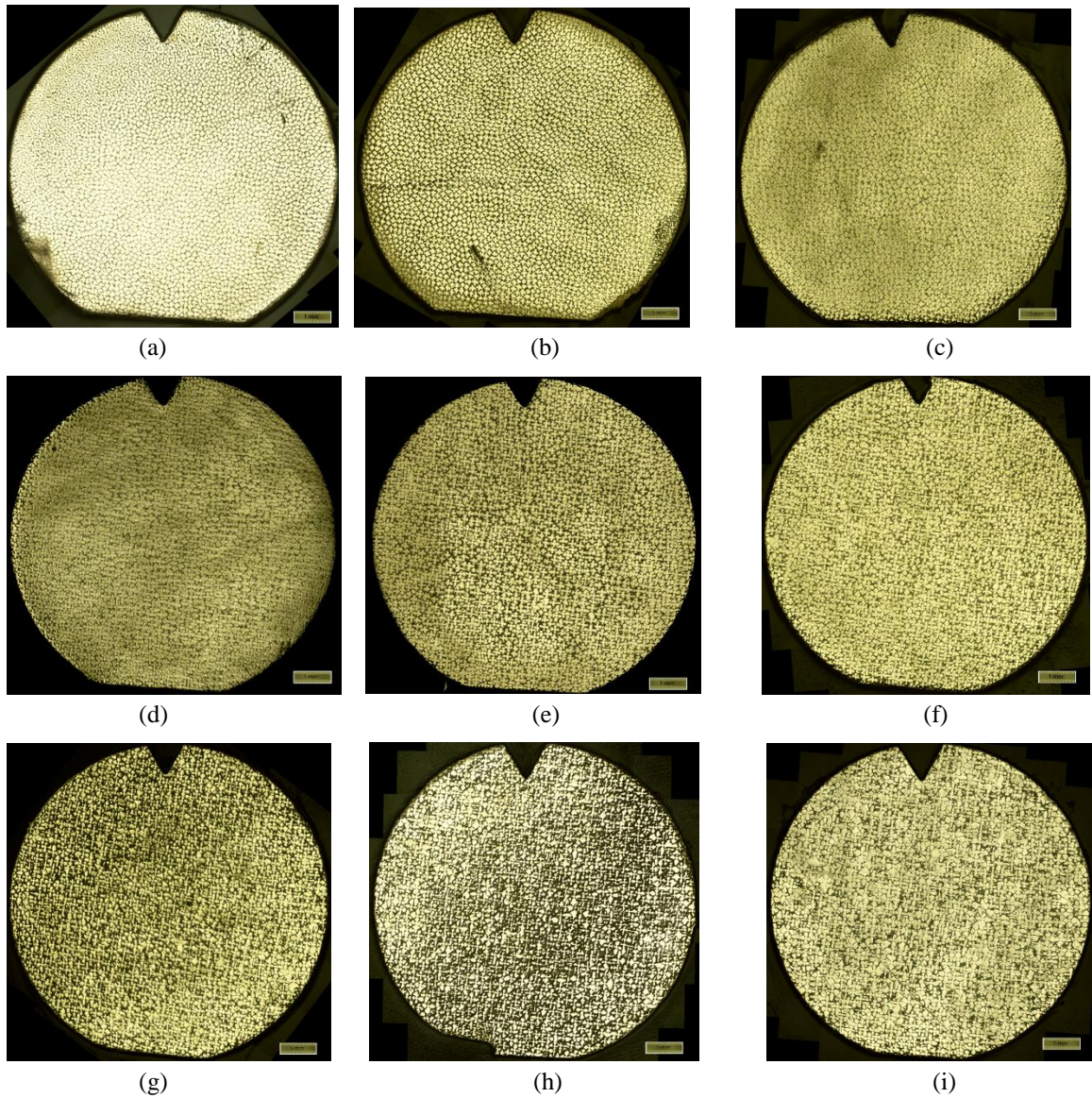


Figure 16. Transverse microstructure of 12_11_17 at different distance away from Te (a) 0.25 cm (b) 0.75 cm (c) 1.75 cm (d) 2.75 cm (e) 3.75 cm (f) 4.75 cm (g) 5.75 cm (h) 6.75 cm (i) 7.75 cm (j) 8.75 cm (k) 9.75 cm (l) 10.75 cm (m) 11.75 cm (n) 12.75 cm (o) 13.75 cm

4.1.2. Gradient Freeze DS at Fast Cooling Rate

Figure 18 shows the transverse microstructures obtained from sample #11_6_17 which was solidified at 4 C/min cooling rate. Figure 19 shows higher magnification views from these sections. The morphology is initially cellular having no branches (Fig.

18(a), 19(a). It shows cell to dendrite transition at approximately 1 cm (Fig. 18(b) and Fig. 19(b)) and formation of side-arms begins at approximately 3 cm (Fig. 18(d) and Fig. 19(d)). Well-branched dendrite arrays are obtained at a distance of about 7 cm (Fig. 18(h) and Fig. 19(h)). In this sample also, the area fraction occupied by the eutectic portion appears to increase as a function of solidification distance. However, at this speed no visible presence of channel segregate is seen along the entire DS length of the sample.



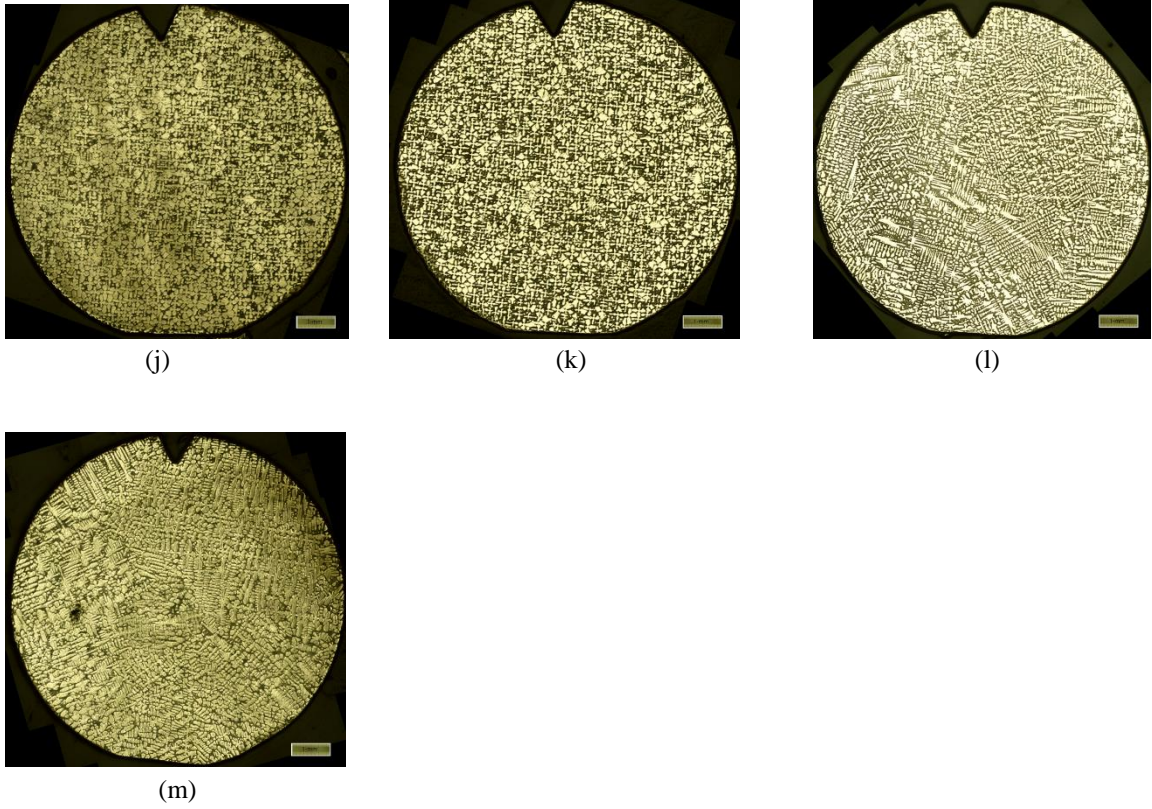
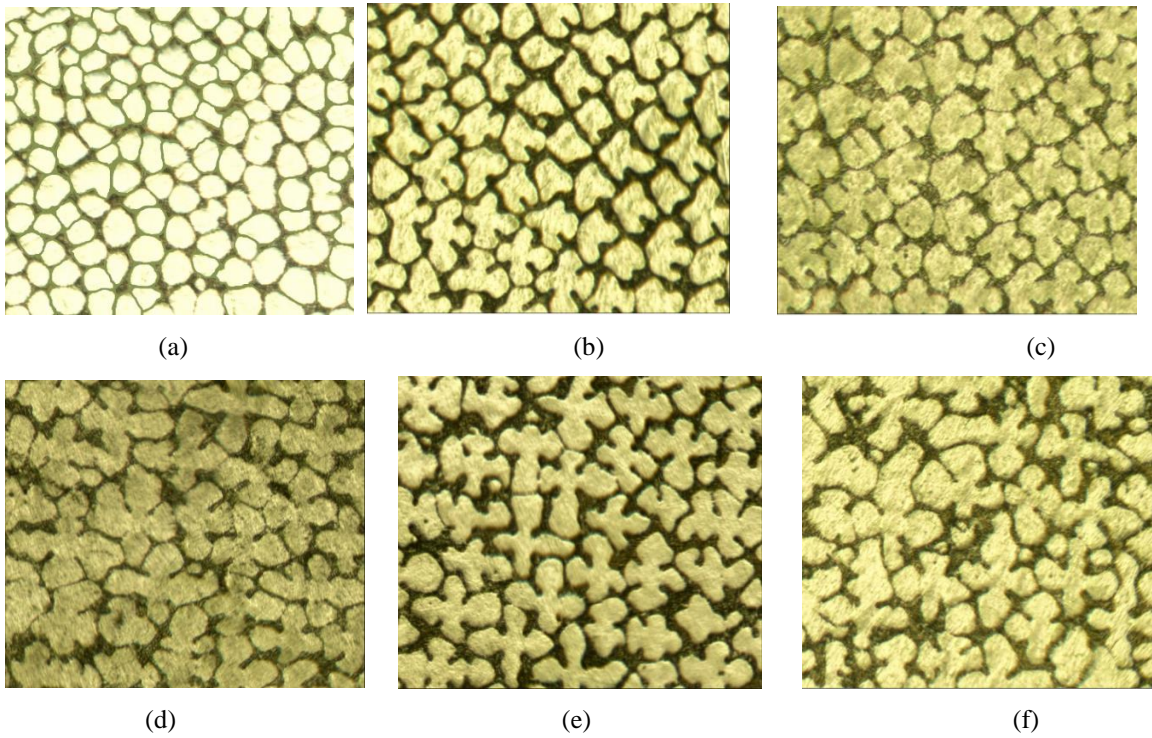


Figure 17. Transverse microstructure of 11_6_17 at different distance away from Te (a) 0.5 cm (b) 1 cm (c) 2 cm (d) 3 cm (e) 4 cm (f) 5 cm (g) 6 cm (h) 7 cm (i) 8 cm (j) 9 cm (k) 10 cm (l) 11 cm (m) 12 cm



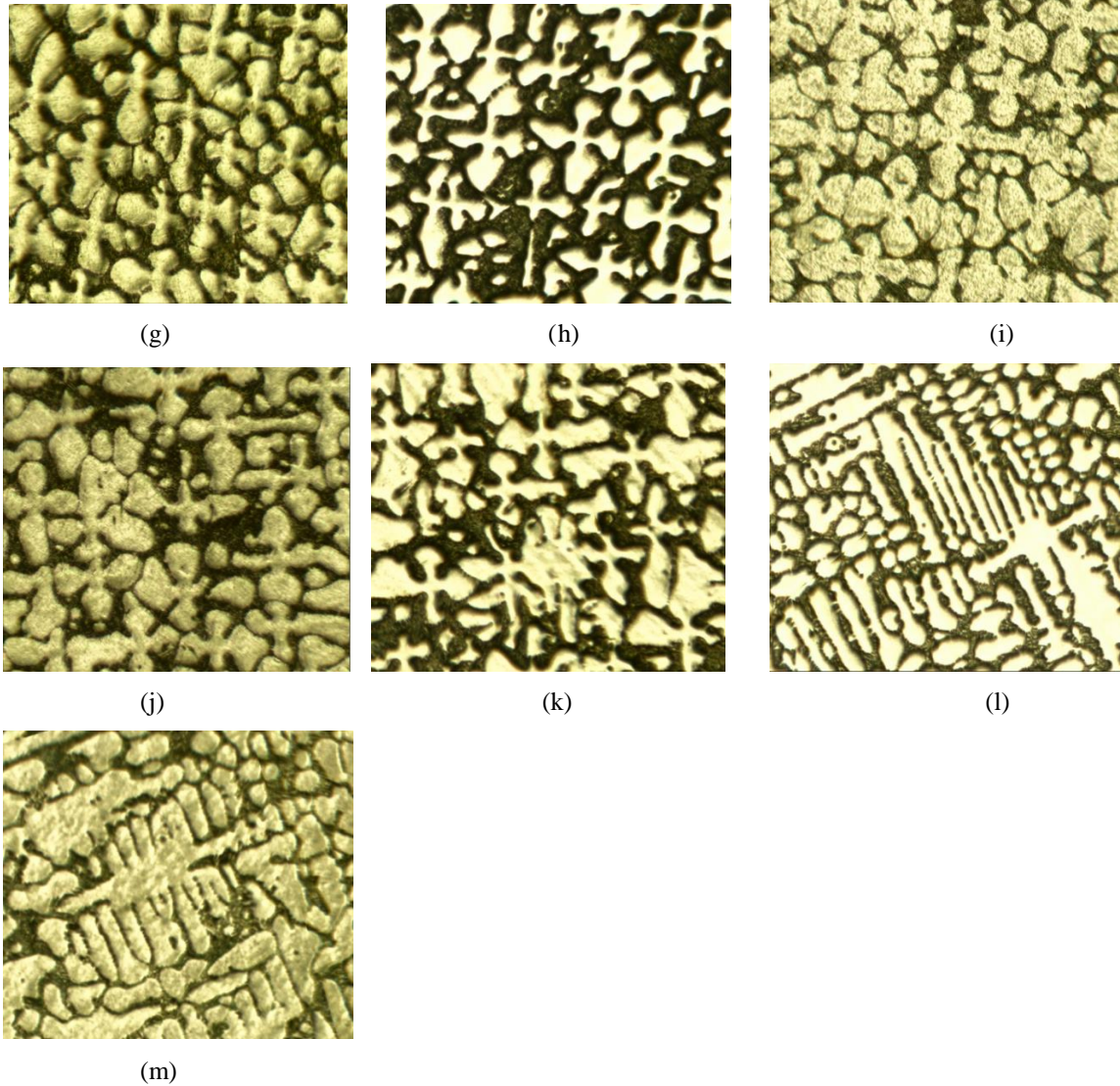


Figure 18. Transverse microstructure of 11_6_17 at different distance away from Te (a) 0.5 cm (b) 1 cm (c) 1 cm (d) 3 cm (e) 4 cm (f) 5 cm (g) 6 cm (h) 7 cm (i) 8 cm (j) 9 cm (k) 10 cm (l) 11 cm (m) 12 cm

	Actual distance from T_E end, (cm)	
	(12_11_17)	(11_6_17)
Primary cell structure	2.75	1
Cell to dendrite structure transformation	4.75	3
Well branched dendrite structure	5.75	4

Table 4 Comparison of dendrite morphology variation with respect to distance for slower and faster cooling rate sample

Table 4 shows that development of dendrite morphology with respect to distance for both slower and faster cooling rate sample. According to the cell structure appears in both cooling rate samples, it appears is much earlier in faster cooling rate than slower cooling rate sample. The same thing is observed where transformation of cell to dendrite structure is appeared and where well branched dendrite structure is observed. Due to faster cooling rate in sample 11_6_17, development of dendrite morphology is much faster than slower cooling rate sample 12_11_17.

4.2. Thermal Gradient and Growth Speed Variation Along DS length

The procedure by which the thermal gradient and growth speed corresponding to the transverse sample locations along the length of the directionally solidified samples were measured for a comparison of primary dendrite spacing and trunk diameters is described below. The thermal profile recorded by the ten thermocouples as a function of time during the furnace cooling period were used to identify the relative distance the of eutectic isotherm (d_L) and the liquidus isotherm (d_E) (with respect to their initial locations at the onset of DS process) as a function of time as the mushy-zone traversed from one end of the sample to the other. These plots can be used to extract the growth speed (cm s^{-1}) and the mushy zone freezing rate (K s^{-1}) as a function of solidification distance. The value of the thermal gradient (K cm^{-1}), can then be determined, because freezing rate = growth speed * thermal gradient. However, because the thermocouple locations are different from the locations where transverse sections were made (typically shown in Figure 11(d)), first 4th degree polynomial fit was made to the eutectic and liquidus isotherm traverse distance versus time data, and then the polynomial parameters were used to back calculate the time at which the eutectic and liquidus isotherms arrived at the

locations where transverse microstructures have been examined. Results are presented below.

4.2.1. High Cooling Rate Sample (sample ID: 11_6_17)

Sample #11_6_17 was solidified at 4°C/min from the furnace temperature of 650 C. Figure 20 shows the temperature profiles recorded by the ten thermocouples with respect to time for this sample. Figure 21 shows a portion extracted from Figure 20 where the temperature profiles are limited to mushy zone freezing range from 290 C ($T_L=288$ C) to 250 C ($T_E=252$ C). Figure 22 plots the distance of the eutectic and liquidus isotherms with respect to T_E at the onset of DS for # 11_6_17. Circles correspond to the thermocouple locations and * correspond to the locations of transverse section. If thermocouple measure profiles (circles) is tried to fit with 3rd degree polynomial, residual value is 542.63. If it tried to fit with 4th degree polynomial, residual value is 308.803 and if it fit with 5th degree polynomial, residual value is 308.802. Then ideal value of residual is obtaining by 4th degree polynomial line and lines are the 4th degree polynomial fit to the thermocouple measured profiles (circles). Table 5. Lists the ID of all the transverse sections, their locations with respect to that of T_E at the onset of DS, and the times when the eutectic and liquidus isotherms arrived at those locations (extracted from Figure 22) for high cooling rate gradient freeze DS (# 11_6_17).

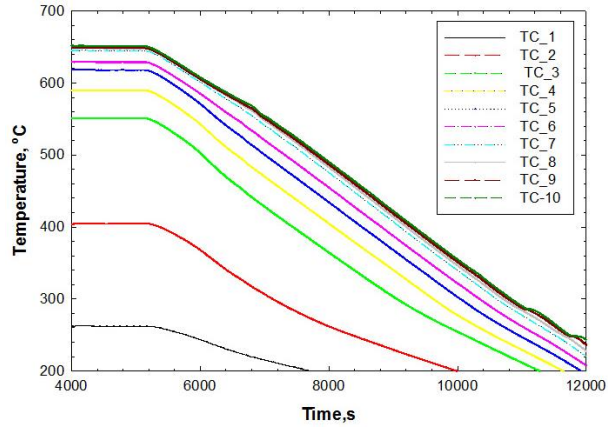


Figure 19. Temperature along the sample length with respect to time for # 11_6_17 sample.

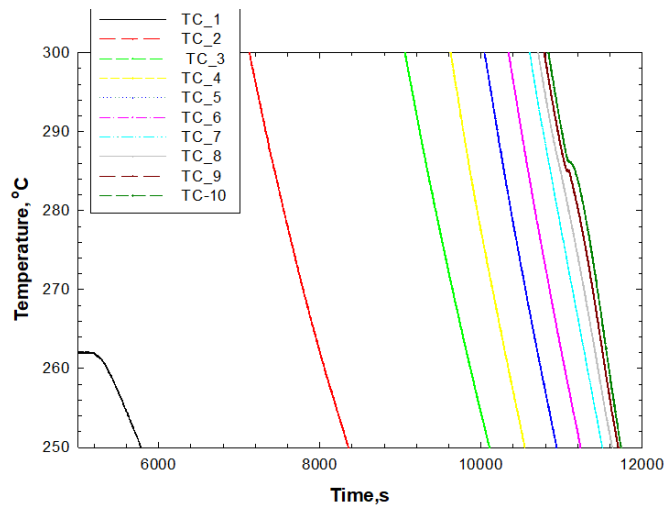


Figure 20. Temperature variation from 290 C (C above the liquidus) to 250 C (C below the eutectic) as a function of time for sample # 11_6_17

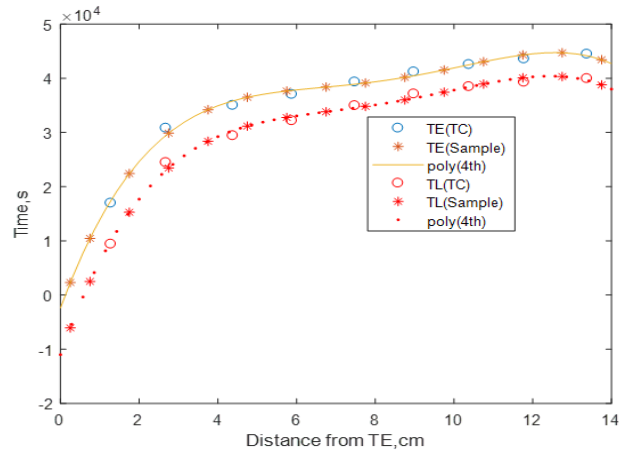


Figure 21. Distance of eutectic and liquidus isotherms with respect to TE at the onset of DS for # 11_6_17. Circles correspond to the thermocouple locations and * correspond to the locations of transverse section. The lines are the 4th degree polynomial fit to the thermocouple measured profiles.

Sample ID (11_6_17)	Distance from Te (cm)	Time when T _L at sample (s)	Time when T _E at sample (s)
1B	0.5	491.058654	1658.118503
1	1	1498.01278	2546.609949
2	2	3015.578532	3888.803872
3	3	4010.957848	4774.291667
4	4	4631.159676	5332.438351
5	5	4999.746882	5671.751824
6	6	5216.836247	5879.882867
7	7	5359.098466	6023.625144
8	8	5479.758149	6148.915199
9	9	5608.593823	6280.832459
10	10	5751.937929	6423.599233
11	11	5892.676823	6560.580711
12	12	5990.250777	6654.284965

Table 5 Locations of transverse samples and the times when the eutectic and liquidus isotherms arrived at those locations (# 11_6_17).

Using data presented in Table 5, the mushy-zone freezing time corresponding to the transverse sample locations were extracted and are plotted in Figure 23. The corresponding mushy-zone cooling rates were then calculated,

$$\text{Mushy zone cooling rate}(K/S) = \left\{ \frac{((TL) - (TE))}{\text{Freezing Time}} \right\}$$

These are presented in Table 6 and are plotted in Figure 24.

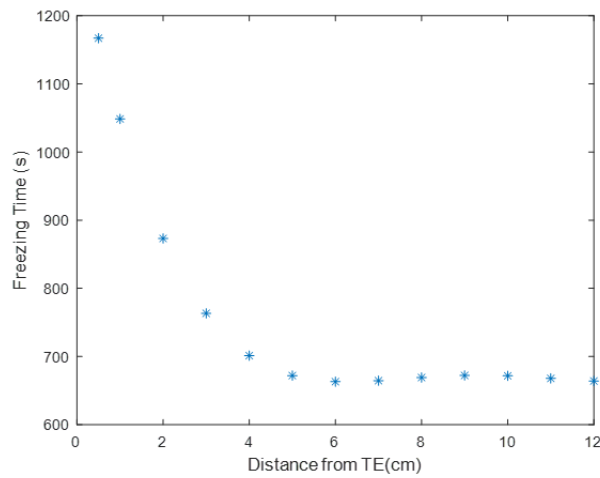


Figure 22. Mushy-zone freezing time versus distance for transverse sample locations (#11_6_17)

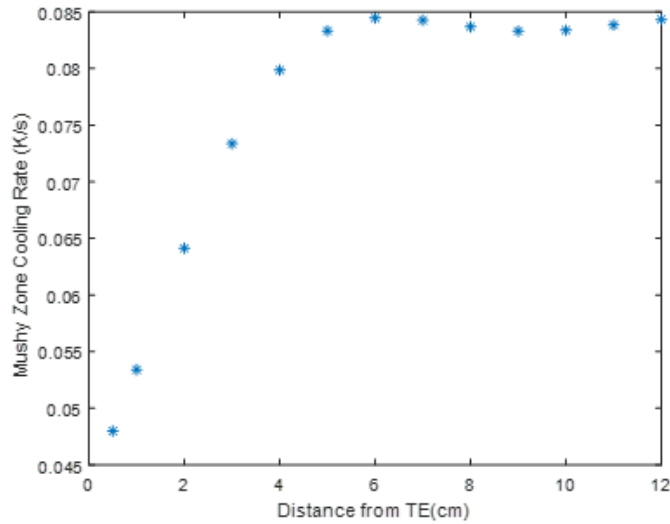


Figure 23. Mushy zone freezing rate with respect to distances of transverse samples (#11_6_17)

Sample ID (11_6_17)	Distance from T _E (cm)	Mushy zone freezing rate (K/s)
1B	0.5	0.04798383
1	1	0.05340468
2	2	0.06413007
3	3	0.0733624
4	4	0.07985413
5	5	0.08333272
6	6	0.08445862
7	7	0.08427051
8	8	0.08368738
9	9	0.08330375
10	10	0.08337536
11	11	0.0838444
12	12	0.08433301

Table 6 Mushy zone freezing rate with respect to distance for transverse samples cut from #11_6_17

The growth speed of the liquidus and eutectic isotherms corresponding to the locations of the transverse sections were obtained by calculating the slopes of the distance vs time plots (calculated from their corresponding polynomial fits (Figure 22)). These growth speeds are presented in Table 7 and are plotted in Figure 25. The mean of these two speeds has been used in comparing the experimentally observed and theoretically predicted values of the primary spacing and trunk diameter later.

Sample ID (11_6_17)	Distance from T _E (cm)	Growth speed at liquidus (cm/s)	Growth speed at Eutectic (cm/s)	Mean growth speed (cm/s)
1B	0.5	0.000454106	0.000514935	0.000485
1	1	0.000545398	0.00061771	0.000582
2	2	0.000812997	0.000916975	0.000865
3	3	0.001273491	0.001424513	0.001349
4	4	0.002101924	0.002312762	0.002207
5	5	0.003595751	0.003833593	0.003715
6	6	0.005922375	0.006004474	0.005963
7	7	0.008029289	0.007776161	0.007903
8	8	0.008214333	0.007926327	0.00807
9	9	0.007299892	0.007226666	0.007263
10	10	0.00680978	0.006925942	0.006868
11	11	0.007820429	0.008108353	0.007964
12	12	0.017664707	0.018397892	0.018031

Table 7 Growth speed of the eutectic and liquidus isotherms vs. distance of the cross-sections with respect to TE at the onset of DS for #11_6_17

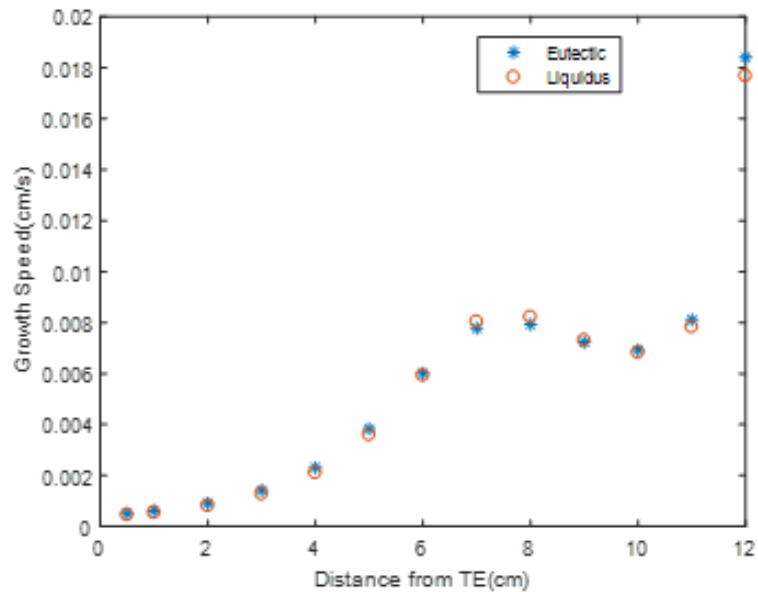


Figure 24. Growth speed with respect to distances of transverse samples (#11_6_17)

The mushy zone freezing rates presented in Table 6 (Figure 24) were used together with the eutectic and liquidus isotherm speed data from Table 7 (Figure 25) to calculate the thermal gradients corresponding to the transverse sample location at the eutectic and liquidus temperatures in the manner described earlier.

$$R \left(\frac{cm}{s} \right) * G \left(\frac{K}{cm} \right) = \text{Mushy zone cooling rate} \left(\frac{K}{s} \right)$$

R = Mean growth rate of liquidus and eutectic, G = Thermal gradient at liquidus or at eutectic, as needed.

Sample ID (11_6_17)	Distance from T _E (cm)	Thermal gradient at liquidus (K/cm)	Thermal gradient at eutectic (K/cm)
1B	0.5	105.6665334	93.18430207
1	1	97.91874098	86.45593106
2	2	78.88108621	69.93652755
3	3	57.60730426	51.50000015
4	4	37.99096648	34.52761091
5	5	23.17532924	21.73749748
6	6	14.26093724	14.06594706
7	7	10.49538793	10.83703282
8	8	10.1879703	10.55815432
9	9	11.41164119	11.52727252
10	10	12.24347204	12.03812463
11	11	10.72120167	10.34049733
12	12	4.774096055	4.583840776

Table 8 Values of Thermal gradient with respect to distances of transverse samples (#11_6_17).

Table 8 gives the calculated values of thermal gradient at each location for liquidus and eutectic. By plotting values of Table 8 thermal gradient plot with respect to distance of sample gives the thermal profile of higher cooling rate sample 11_6_17

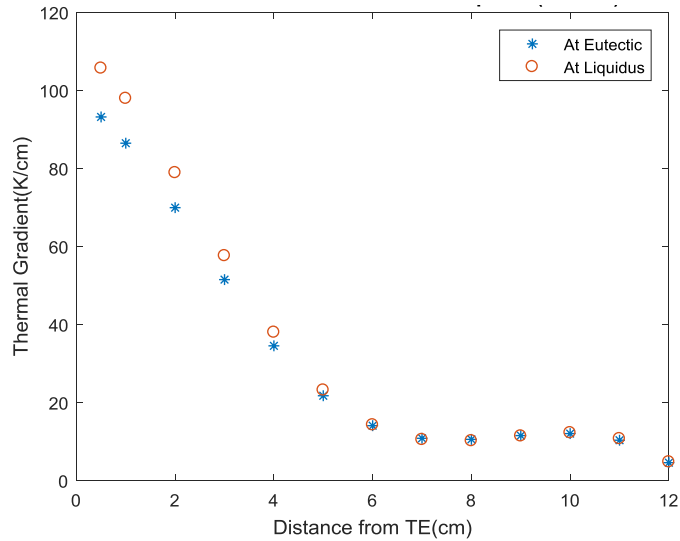


Figure 25. The liquidus and eutectic thermal gradients with respect to distances of transverse samples (#11_6_17).

4.2.2. Slow Cooling Rate Sample (sample ID: 12_11_17)

Sample #12_11_17 was solidified at 0.5°C/min from the furnace temperature of 650°C, which is slower cooling rate sample. Figure 27 shows the temperature recorded by the ten different thermocouples with respect to time for this sample. Mushy zone freezing range is from 290 C ($T_L= 288$ C) liquidus to 250 C ($T_E=252$ C) eutectic and Figure 28 shows a portion extracted from Figure 28 where temperature profile is limited to mushy zone range. Figure 29 plots the distance of the eutectic and liquidus isotherms with respect to T_E at the onset of DS for 12_11_17. Circles correspond to the thermocouple locations and * correspond to the locations of transverse section. If thermocouple measure profiles (circles) is tried to fit with 3rd degree polynomial, residual value is 4171.02. If it tried to fit with 4th degree polynomial, residual value is 2137.66

and if it fit with 5th degree polynomial, residual value is 683.58. Then ideal value of residual is obtaining by 4th degree polynomial line and lines are the 4th degree polynomial fit to the thermocouple measured profiles (circles). Table 4. Lists the ID of all the transverse sections, their locations with respect to that of T_E at the onset of DS, and the times when the eutectic and liquidus isotherms arrived at those locations (extracted from Figure 29) for slow cooling rate gradient freeze DS (12_11_17).

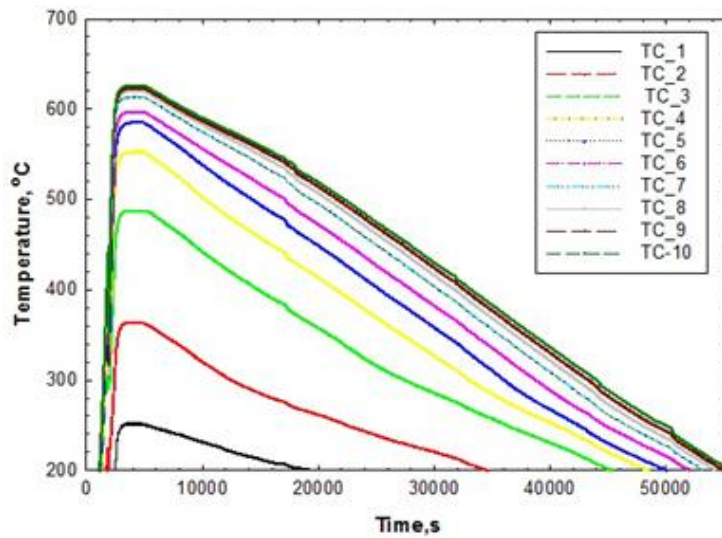


Figure 26. Temperature along the sample length with respect to time for #12_11_17 sample

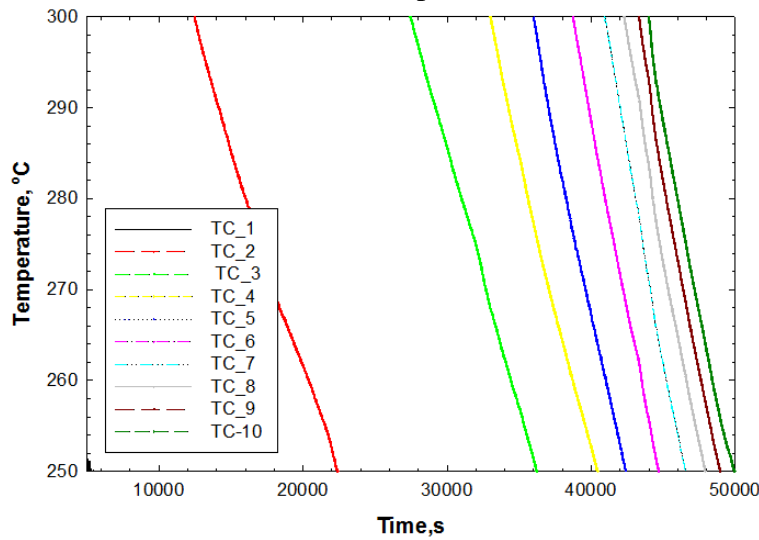


Figure 27. Temperature variation from 290 C (C above the liquidus) to 250 C (C below the eutectic) as a function of time for sample #12_11_17

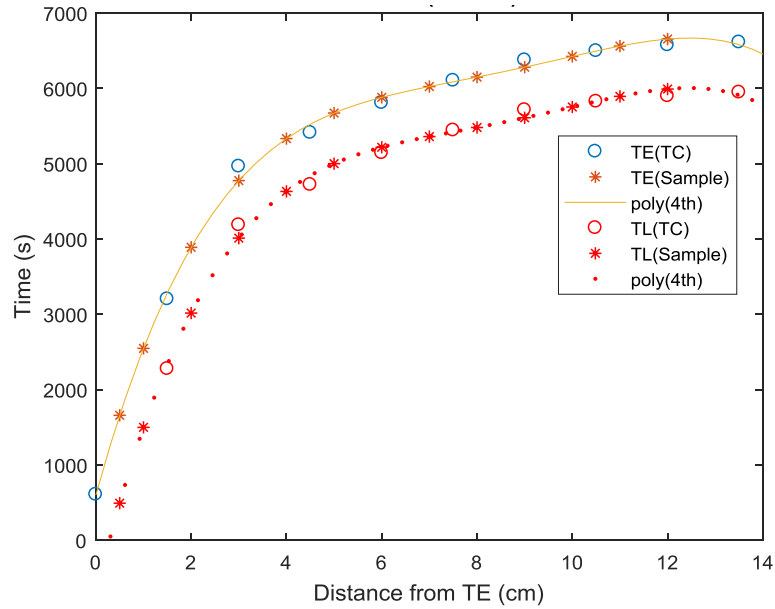


Figure 28. Distance of eutectic and liquidus isotherms with respect to TE at the onset of DS for #12_11_17. Circles correspond to the thermocouple locations and * correspond to the locations of transverse section. The lines are the 4th degree polynomial fit to the thermocouple measured profiles.

Sample ID (12_11_17)	Distance from T _E (cm)	Time when T _L at sample (s)	Time when T _E at sample (s)
1B	0.25	-6.07E+03	2.32E+03
1	0.75	2.51E+03	1.05E+04
2	1.75	1.53E+04	2.24E+04
3	2.75	2.34E+04	2.99E+04
4	3.75	2.84E+04	3.42E+04
5	4.75	3.12E+04	3.65E+04
6	5.75	3.28E+04	3.77E+04
7	6.75	3.38E+04	3.84E+04
8	7.75	3.48E+04	3.91E+04
9	8.75	3.60E+04	4.02E+04
10	9.75	3.74E+04	4.15E+04
11	10.75	3.89E+04	4.31E+04
12	11.75	4.01E+04	4.43E+04
13	12.75	4.03E+04	4.47E+04
14	13.75	3.88E+04	4.34E+04

Table 9 Locations of transverse samples and the times when the eutectic and liquidus isotherms arrived at those locations (#12_11_17).

Using data presented in Table 9, the mushy-zone freezing time corresponding to the transverse sample locations were extracted and are plotted in Figure 30. As discussed earlier, using the data points of freezing time and mushy zone temperature difference corresponding mushy zone cooling rate were calculated which tabulated in Table 10 and plotted in Figure 31.

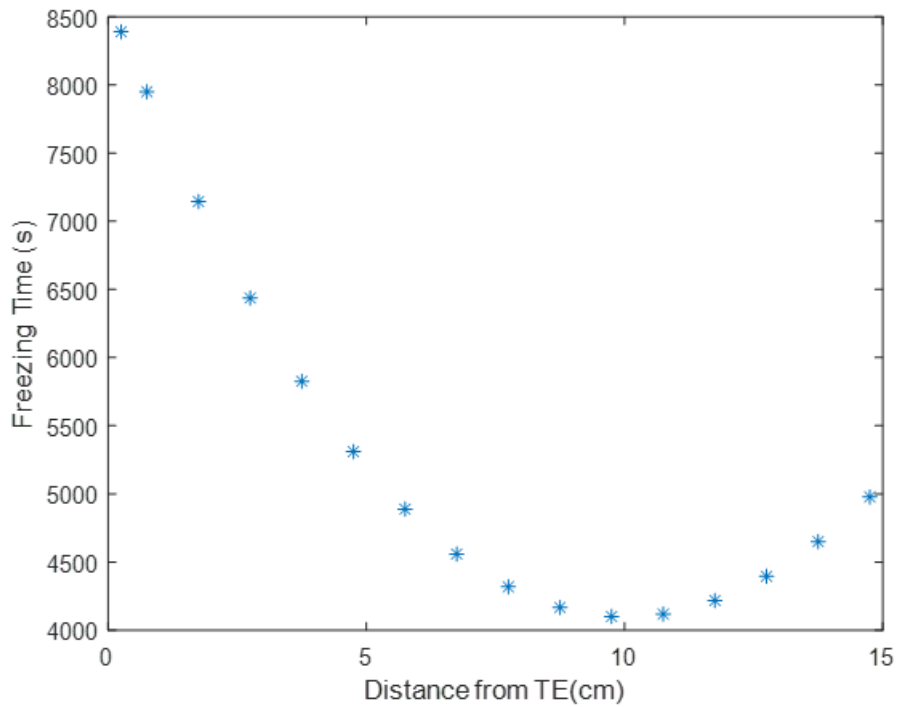


Figure 29. Mushy-zone freezing time verses distance for transverse sample locations (#12_11_17)

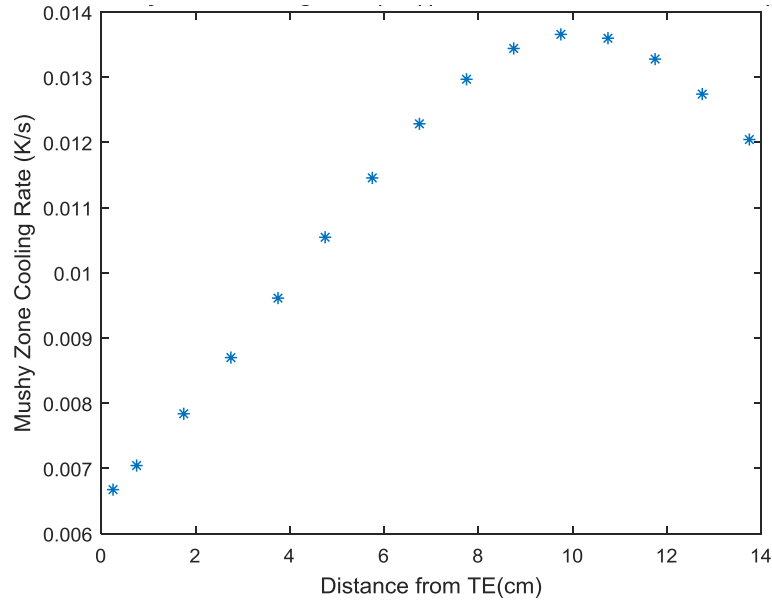


Figure 30. Mushy zone cooling rate with respect to distance for 12_11_17

Sample ID (12_11_17)	Distance from T _E (cm)	Mushy zone cooling rate (K/s)
1B	0.25	0.0067
1	0.75	0.007
2	1.75	0.0078
3	2.75	0.0087
4	3.75	0.0096
5	4.75	0.0105
6	5.75	0.0115
7	6.75	0.0123
8	7.75	0.013
9	8.75	0.0134
10	9.75	0.0137
11	10.75	0.0136
12	11.75	0.0133
13	12.75	0.0127
14	13.75	0.012

Table 10 Values of Mushy zone cooling rate with respect to distance for 12_11_17

The growth speed of the liquidus and eutectic isotherms corresponding to the locations of the transverse sections were obtained by calculating the slopes of the distance vs time plots (calculated from their corresponding polynomial fits (Figure 31)). These growth speeds are presented in Table-11 and are plotted in Figure 32. The mean of these two speeds has been used in comparing the experimentally observed and theoretically predicted values of the primary spacing and trunk diameter later.

Sample ID (12_11_17)	Distance from T _E (cm)	Growth speed at liquidus (cm/s)	Growth speed at Eutectic (cm/s)	Mean growth speed (cm/s)
1B	0.25	5.31E-05	5.58E-05	5.44385E-05
1	0.75	6.43E-05	6.80E-05	6.61425E-05
2	1.75	9.78E-05	1.06E-04	0.000101656
3	2.75	1.58E-04	1.76E-04	0.00016664
4	3.75	2.70E-04	3.19E-04	0.000294745
5	4.75	4.85E-04	6.28E-04	0.000556755
6	5.75	8.19E-04	0.0012	0.00100948
7	6.75	0.001	0.0015	0.00125
8	7.75	9.35E-04	0.0011	0.00101758
9	8.75	7.55E-04	8.23E-04	0.000788935
10	9.75	6.62E-04	6.72E-04	0.000667175
11	10.75	7.08E-04	6.79E-04	0.000693615
12	11.75	0.0012	0.001	0.0011
13	12.75	-0.002	-0.0035	-0.00275
14	13.75	-3.63E-04	-4.06E-04	-0.0003848

Table 11 Growth speed of the eutectic and liquidus isotherms vs. distance of the cross-sections with respect to T_E at the onset of DS for #12_11_17

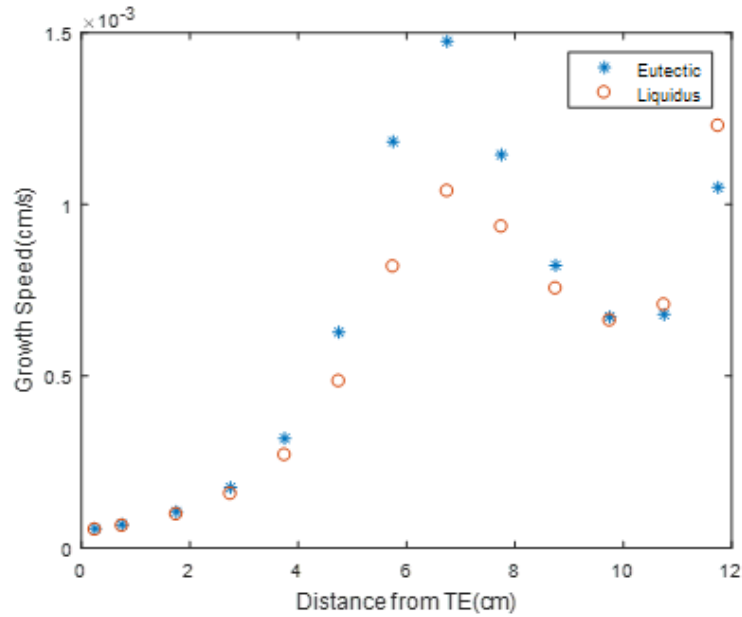


Figure 31. Growth speed with respect to distance of sample (#12_11_17)

The mushy zone freezing rates presented in Table-10 (Figure 31) were used together with the eutectic and liquidus isotherm speed data from Table 11 (Figure 32) to calculate the thermal gradients corresponding to the transverse sample location at the eutectic and liquidus temperatures in the manner described earlier.

Table 12 gives the calculated values of thermal gradient at each location for liquidus and eutectic. By plotting values of Table 12 thermal gradient plot with respect to distance of sample gives the thermal profile of higher cooling rate sample 12_11_17.

Sample ID (12_11_17)	Distance from T _E (cm)	Thermal gradient at liquidus (K/cm)	Thermal gradient at liquidus (K/cm)
1B	0.25	125.6996	119.6594
1	0.75	109.5921	103.5682
2	1.75	80.1859	74.2564
3	2.75	55.2323	49.4984
4	3.75	35.5414	30.1292
5	4.75	21.7293	16.7879
6	5.75	13.9888	9.6842
7	6.75	11.8292	8.3312
8	7.75	13.8678	11.3309
9	8.75	17.7984	16.3391
10	9.75	20.634	20.3104
11	10.75	19.2134	20.0139
12	11.75	10.8087	12.6543
13	12.75	-6.4012	-3.6423
14	13.75	-33.1549	-29.6452

Table 12 Values of Thermal gradient with respect to distance for 12_11_17

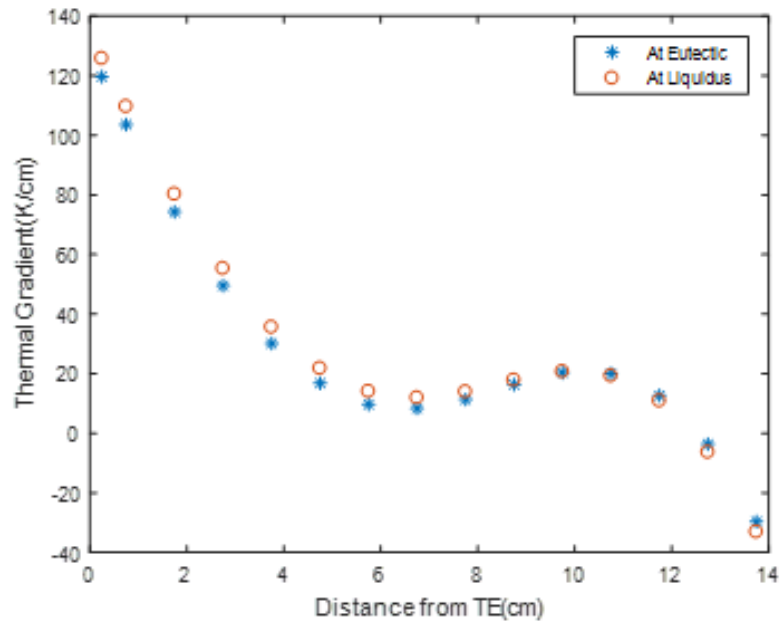


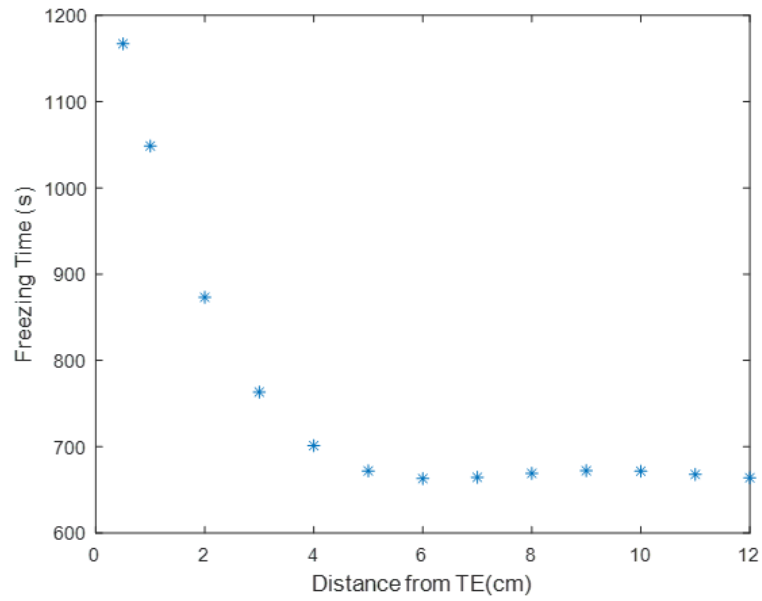
Figure 32. Thermal gradient verses Distance on sample 12_11_17

4.3. Dependence of the solidification behavior as a function of furnace cooling rate during gradient freeze DS process.

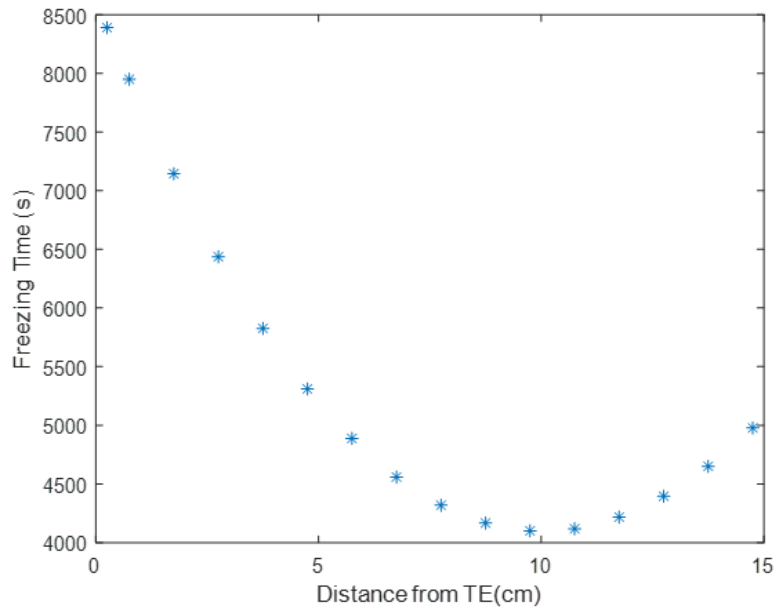
Figure 34 compares the mushy-zone freezing time of the two Pb-5.8 Sb samples Directional solidified at two furnace cooling rates, 4 K/min (11_6_17) and at 0.5 K/min (12_11_17). For both samples the freezing time decreases as the liquid solid interface moves from the bottom end of the melt column towards its top end, because the heat is being extracted only from the bottom end which is maintained at room temperature by the gallium bath. As the length of the solidified portion of the alloy increases it provides additional resistance to the heat transfer at the cold end and the actual thermal gradient in the mushy-zone up above decreases. The heat is also being extracted from the hot end of the sample because radially (as shown schematically in Figure 35). It becomes rate controlling towards the end of the DS as compared with the little heat still being extracted from the bottom. The melt still left to solidify begins to undercool and solidify in a non-directional manner.

If the furnace cooling rates were actually felt throughout the length of the actual sample during directional solidification then one would have expected a mushy-zone freezing time of 540 and 4320 S for the two Pb-5.8Sb alloy samples #11_6_17 and 12_11_17, respectively. Figure 34 shows those actual freezing times are much larger than that especially in the beginning of DS. Only after about 6 cm after onset of DS till about 11 cm of DS a reasonably constant freezing rate is being maintained and one can assume a steady state growth condition. During the initial 6-cm of DS the growth conditions are transient. This is also reflected in the thermal gradient and growth speed variation plots shown in Figure 36 and 37. Therefore comparison of dendrite morphology with

predictions from theoretical models would make sense only for transverse sections from about 6 cm to 11 cm distances.



(a)



(b)

Figure 33. Effect of furnace cooling rate on the mushy-zone freezing time at transverse sections located at increasing distance from TE at the onset of DS. (a) #11_6_17, (4 °C/min) (b) # 12_11_17, (0.5°C /min).

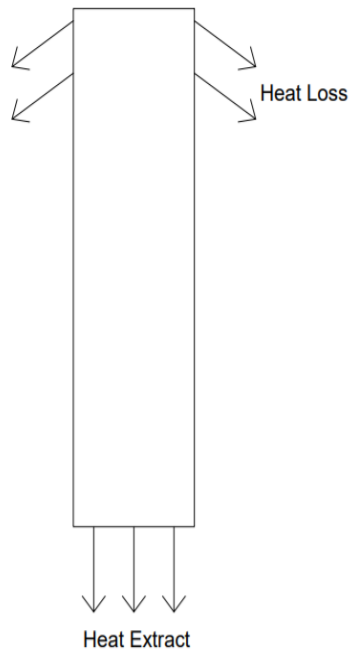


Figure 34. Heat extraction from the top of the ampoule region becomes more dominant as compared with that from the bottom cold end of the sample as liquid-solid interface moves towards the top and the liquid left is at relatively low temperatures.

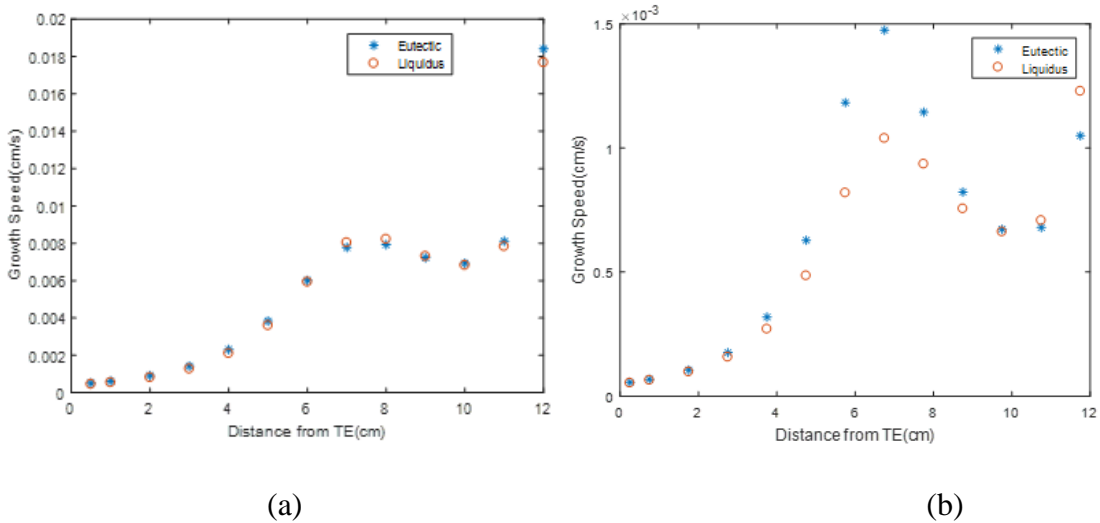


Figure 35. Effect of furnace cooling rate on the eutectic and liquidus isotherm speeds as a function of distance from TE at the onset of DS (a) #11_6_17 (4 C/min) (b) # 12_11_17 (0.5 C/min).

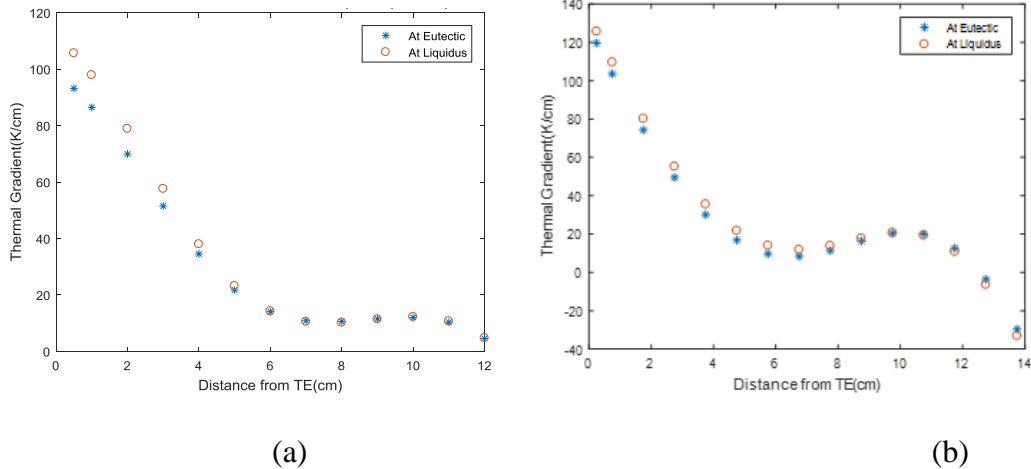


Figure 36. Effect of furnace cooling rate on the eutectic and liquidus isotherm thermal gradient as a function of distance from TE at the onset of DS (a) #11_6_17 (4 C/min) (b) #12_11_17 (0.5 C/min).

4.4. Macrosegregation along the DS length

Figure 38 plots the fraction eutectic with respect to solidification distance for the two samples, one cooled at 0.5 C/min and the other at 4 C/min. The fraction eutectic increases with increasing solidification distance implying that the melt column poor in the solute continuously gets richer in antimony content.

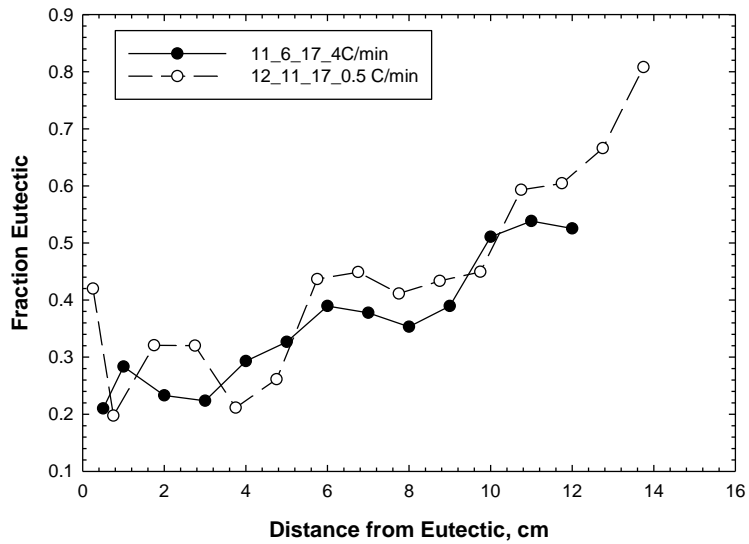


Figure 37. Fraction eutectic verses distance from eutectic

The fraction eutectic values were used in the following relationship to obtain the mean solid composition on each transverse section (C_s):

$$C_s = \{-3.5109 * (f_s)^2 + 13.4846 * (f_s) + 0.801862\}$$

Here, f_s is the fraction volume solidified. Since the alloy melt composition (C_o) was 5.8 % Sb, which is also the mean of C_s across the entire sample length the C_s values calculated from the above relationship were back calibrated, and the ratio C_s/C_o is plotted as a function of fraction solidified in Figure 39. This macrosegregation is caused by the “plume” type of thremosolutal convection which makes the solute rich melt from the bottom of the mushy-zone to move towards the array tips where it mixes with rest of the bulk melt above. This results in a continuous solute enrichment along the DS length. In the absence of such convection the C_s/C_o value would be expected to remain unity along the DS length.

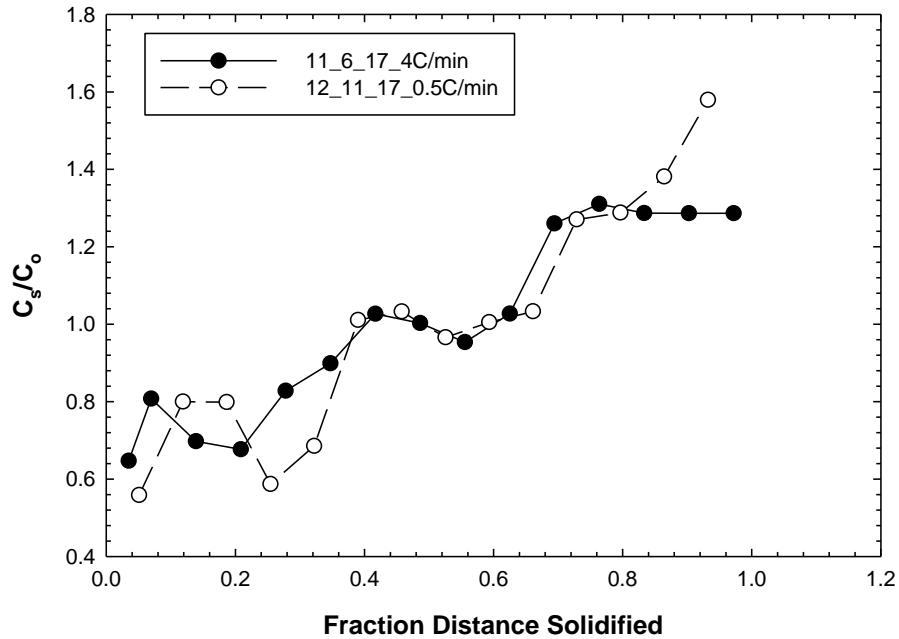


Figure 38. Longitudinal macrosegregation (C_s/C_o) as a function of fraction solidified (f_s)

Such macrosegregation has been shown to follow a $C_s/C_o = k_e (1-f_e)^{k_e-1}$ relationship [10] where k_e is termed as effective partition coefficient. The effective partition coefficient can be obtained from the intercept and the slope of a $\log(C_s/C_o)$ vs $\log(I-f_s)$ plot after a linear regression fit to the experimental data. The k_e value increases with increasing intensity of thermosloutal convection. Figure 40 shows the linear regression fit for the $\log(C_s/C_o)$ vs $\log(I-f_s)$ data for the two samples examined in this study. Average k_e values obtained from the slope and that from the intercept for #11_6_17 is 0.6374 and for the slower cooled sample #12-11-17 it is 0.7757. There is large scatter in the data, therefore, it is not possible to make definite conclusion, but the mictostructural observations (presence of “channel segregates in the slow cooled sample, vs their absence in the faster cooled sample) does suggest that there is more intense convection in the slower cooled sample.

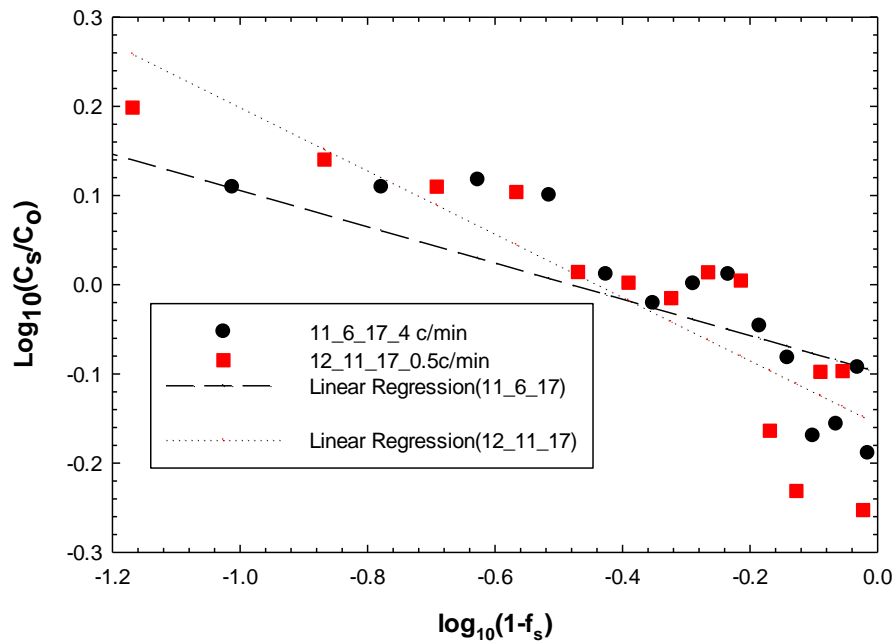
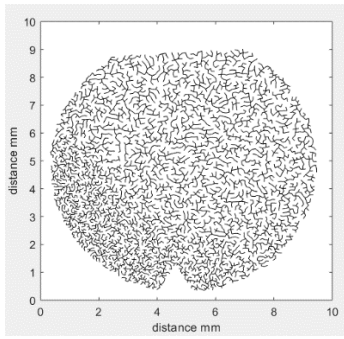


Figure 39. $\log(C_s/C_o)$ vs. $\log(I-f_s)$

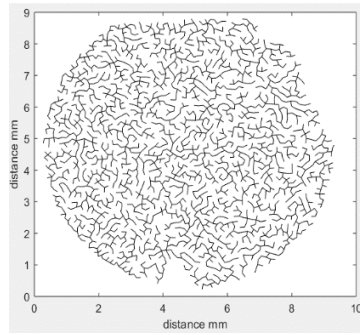
4.5. Comparison with Theoretical Predictions

4.5.1. Minimum Spanning Tree Spacing

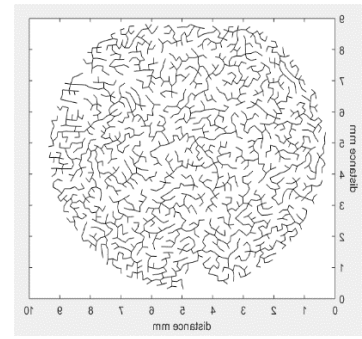
Figure shows the minimum spanning trees obtained on the various cross sections of the two samples examined in this study.



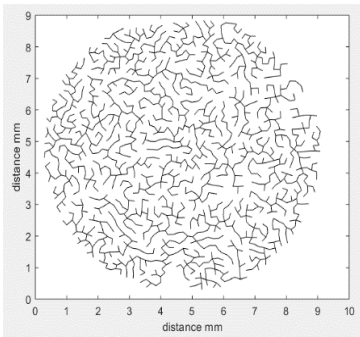
(a)



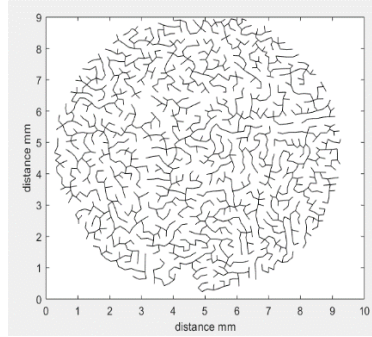
(b)



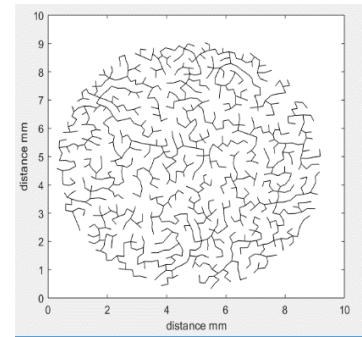
(c)



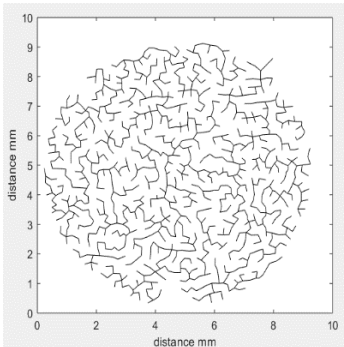
(d)



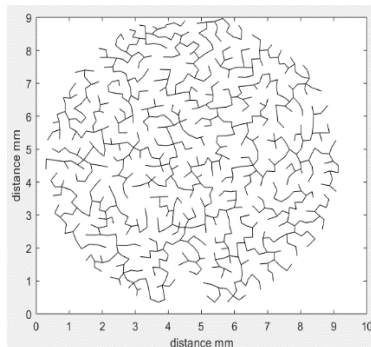
(e)



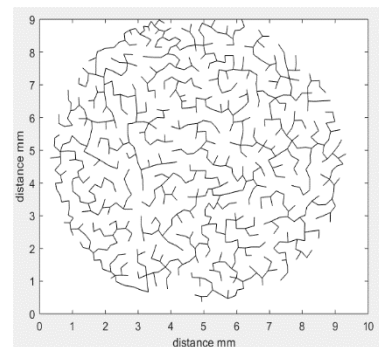
(f)



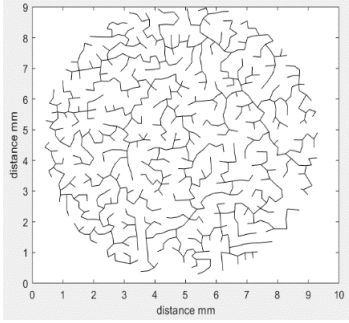
(g)



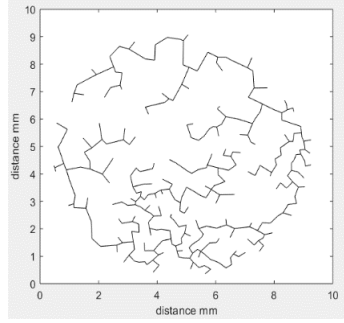
(h)



(i)

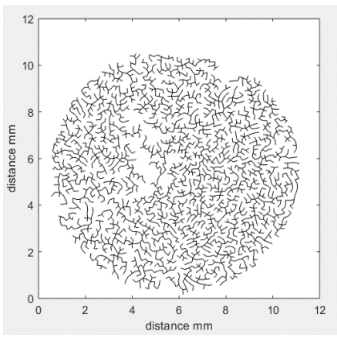


(j)

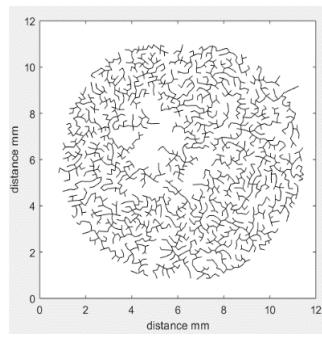


(k)

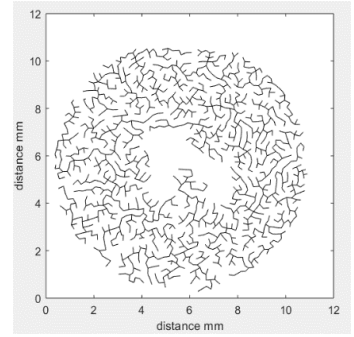
Figure 40. Minimum spanning tree for #11_6_17 at various location from heat extraction end (a) 1 cm (b) 2 cm (c) 3 cm (d) 4 cm (e) 5 cm (f) 6 cm (g) 7 cm (h) 8 cm (i) 9 cm (j) 10 cm (k) 11 cm



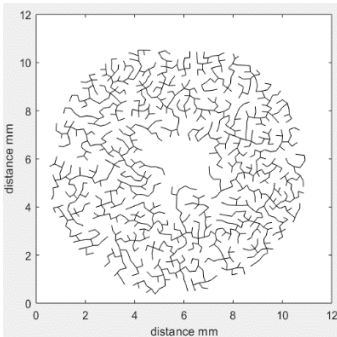
(a)



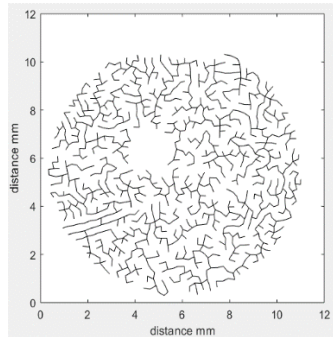
(b)



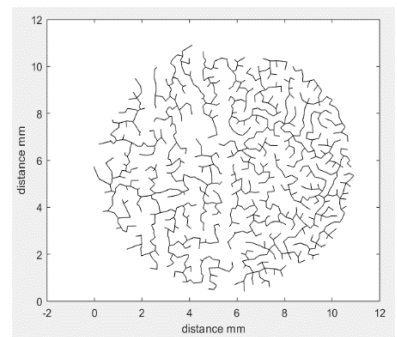
(c)



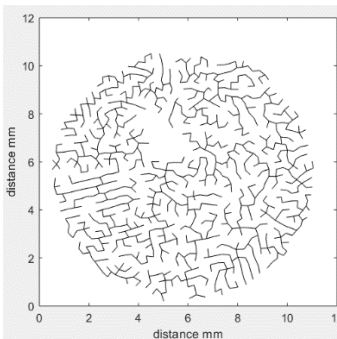
(d)



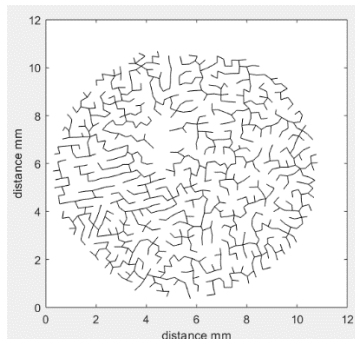
(e)



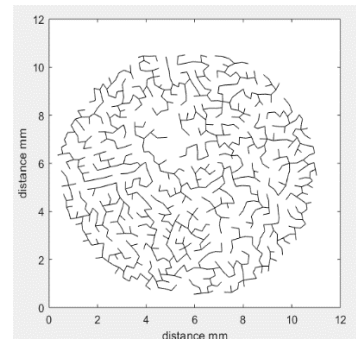
(f)



(g)



(h)



(i)

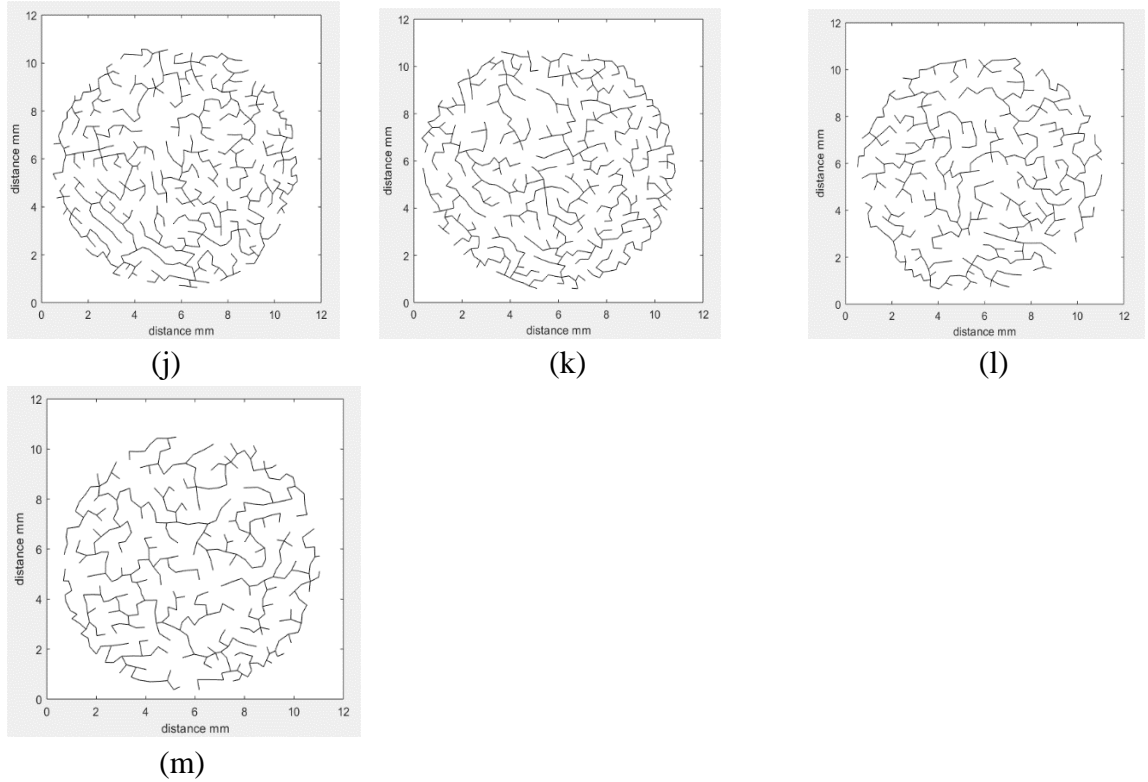
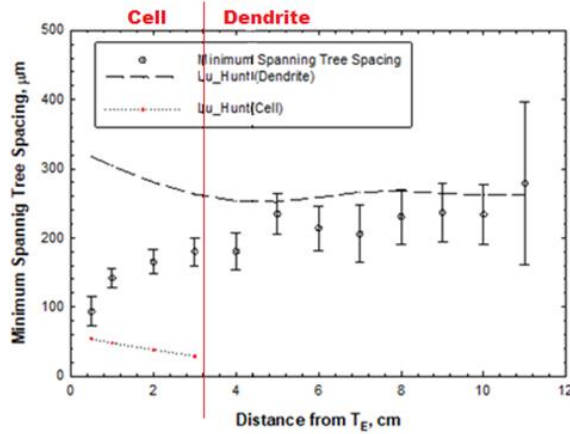


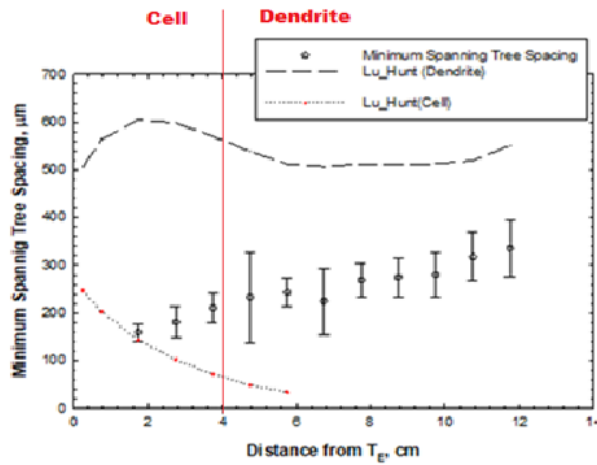
Figure 41. Minimum spanning tree for #12_11_17 at various location from heat extraction end (a) 1.75 cm (b) 2.75 cm (c) 3.75 cm (d) 4.75 cm (e) 5.75 cm (f) 6.75 cm (g) 7.75 cm (h) 8.75 cm (i) 9.75 cm (j) 10.75 cm (k) 11.75 cm (l) 12.75 cm (m) 13.75 cm

Figure 40 shows the variation in Minimum Spanning Tree primary spacing with solidification distance for (a) 4 C/min cooling rate (sample #11_6_17) and (b) 0.5 C/min cooling rate (sample#12_11_17). The symbols correspond to the mean MST spacing with one standard deviation. The dashed lines are primary spacings predicted for Hunt-Lu [18] model for dendrite morphology and the dotted lines are the Hunt-Lu prediction for cell morphology. The distances at which the cell to dendrite transition was observed are indicated by the red vertical line. Both samples show an initial increase in the spacing as the morphology changes from cellular, to dendrites having only rudimentary side arms to well branched dendrites with increasing solidification distance. The cells have much smaller spacing as compared with dendrites, as expected from theoretical models [18].

For dendritic morphologies the experimentally observed MST primary spacings are smaller than those predicted from the theoretical model which assumes only a pure diffusive transport environment during DS. There is a larger deviation from theoretical predictions for dendrites formed in the slower cooling rate sample as compared with the faster cooling rate one.



(a)

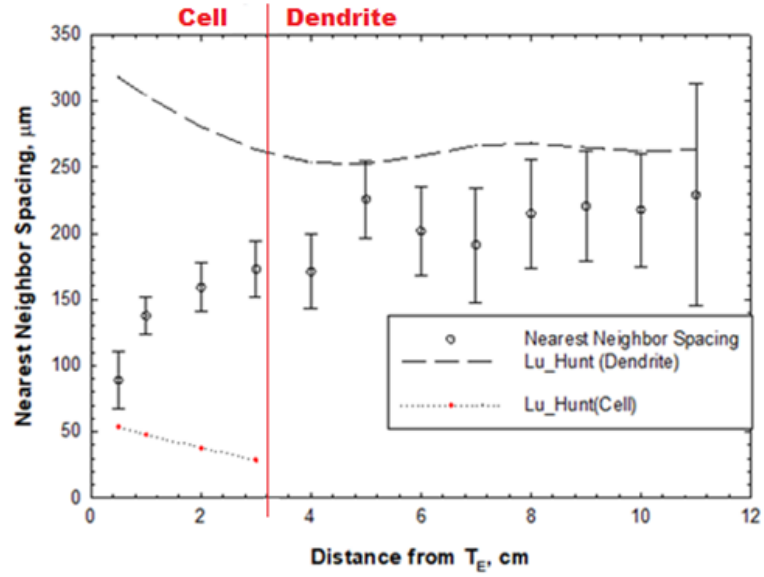


(b)

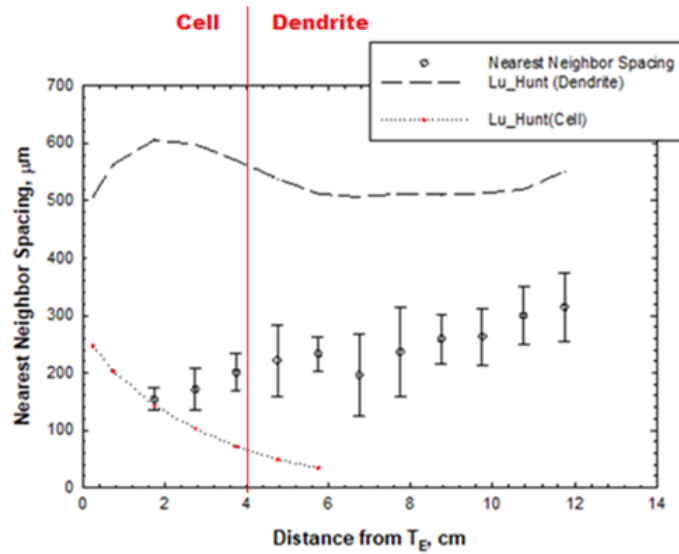
Figure 42. Variation in Minimum Spanning Tree primary spacing with solidification distance. (a) 4 C/min cooling rate (sample #11_6_17) and 0.5 C/min cooling rate (sample#12_11_17). The dashed line is primary spacing predicted for Hunt-Lu [18] model for dendrite morphology and the dotted line is Hunt-Lu prediction for cell morphology. The distance at which cell to dendrite transition was observed is indicated by the red vertical line.

4.5.2. Nearest Neighbor Spacing (NNS)

Figure 41 shows the variation in nearest neighbor primary dendrite spacing as a function of increasing solidification distance for the (a) 4 C/min cooling rate (sample #11_6_17) and (b) 0.5 C/min cooling rate (sample#12_11_17). The mean spacing and one standard deviation for the experimental measurements are plotted in these figures. The dashed lines are predicted values from the Hunt-Lu [18] model for dendrite morphology, and the dotted lines are prediction for the cell morphology. The vertical red lines show the distances at which the cell to dendrite transition was observed. Both samples show an initial increase in the spacing as the morphology changes from cells, to dendrites having only rudimentary side arms to the well branched dendrites as liquid-solid interface moves from the cold end to the hot end of the sample during gradient freeze DS process. The cells have much smaller spacing as compared with dendrites; this is expected from the theoretical models [18]. For dendritic morphologies the experimentally observed nearest neighbor spacings are, however, smaller than those predicted from the Hunt-Lu model. The deviation from theoretical predictions is much larger in the slower cooling rate sample (Figure 41(b) vs. Figure 41(a)) as compared with the faster cooling rate one.



(a)



(b)

Figure 43. Variation in nearest neighbor primary spacing with solidification distance. (a) 4 C/min cooling rate (sample #11_6_17) and 0.5 C/min cooling rate (sample#12_11_17). The dashed line is Hunt-Lu [18] predictions for dendrite morphology and the dotted line is Hunt-Lu prediction for cell morphology. The distance at which cell to dendrite transition was observed is indicated by the red vertical line.

Figure 42 plots the ratio of the experimentally observed nearest neighbor spacing and that predicted from the Hunt-Lu model for “dendrite” morphology for the slow

cooled and fast cooled samples. The ratio expected would be unity if the gradient freeze DS had occurred under purely diffusive transport conditions. It can be inferred from this figure that plume type thermo-solutal convection is responsible for the observed decrease in the primary dendrite spacing. The extent of decrease is much larger in the slower cooled sample because there was more intense convection in these samples as also indicated by the transverse microstructures described earlier.

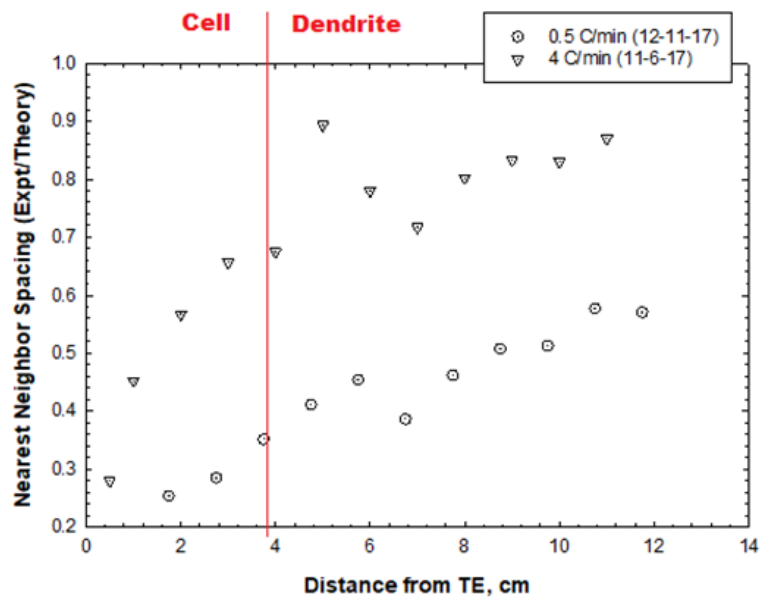
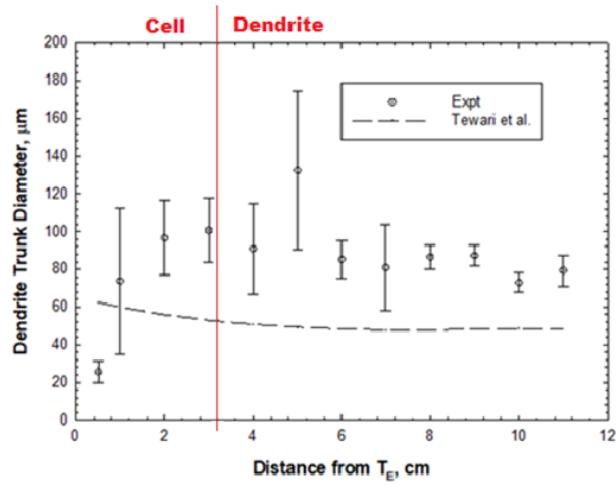


Figure 44. Ratio of the experimentally observed nearest neighbor primary spacing to that predicted from Hunt-LU model for dendrite morphology during DS.

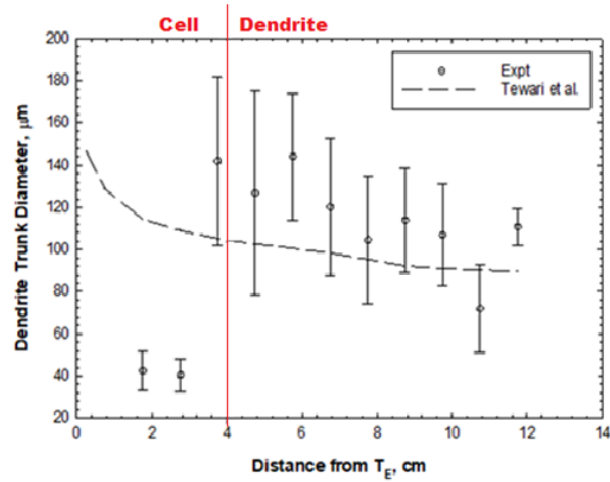
4.5.3. Trunk Diameter (TD)

Figure 43 shows the experimentally observed Primary Dendrite Trunk diameter as a function of solidification distance for the two cooling rate samples examined in this study, (a) 4 C/min cooling rate # 11_6_17, and (b) 0.5 C/min cooling rate #12_11_17. The mean and one standard deviation values are indicated by the data points. The dotted line is the trunk diameter predicted from the analytical model [19]. Since the model is valid only for the dendrite morphology and not for the cells, only the data to the

right of the cell-dendrite transition should be compared with the model predictions. The experimentally observed trunk diameters are larger than those predicted from theory. The difference again may be attributed to the thermosolutal convection present during gradient freeze DS of these Pb-5.8Sb alloy samples.



(a)



(b)

Figure 45. Variation in Primary Dendrite Trunk diameter as a function of solidification distance. (a) 4 C/min cooling rate sample# 11_6_17 (b) 0.5 C/min cooling rate sample #12_11_17. The dotted line is the trunk diameter predicted from analytical model [19] which is strictly valid only for the dendrite morphology and not for the cells.

CHAPTER V

SUMMARY

Directional solidification (DS) is the process of solidifying a metal alloy from one end to another resulting in aligned primary dendrites which are branched tree like features. Alignment of primary dendrites along [100] direction and their uniformity and distribution along the DS length determines the mechanical properties. These properties are especially important for single crystal turbine blade applications in modern gas turbine engines. Convection during solidification plays an important role in formation of detrimental defects, such as, misaligned grains, non-uniformity of dendrites and composition inhomogeneity. Purpose of this study was to examine the microstructural evolution of primary dendrites during “Gradient Freeze DS process” in cylindrical Pb-5.8% Sb alloy samples to generate the ground-based research data to support a future microgravity experiment on the Space Station in a convection free environment. Pb-5.8Sb was selected for this study because of its ease of processing and availability of physical property data which will be required for predicting the dendrite morphology parameters, such as, primary dendrite spacing and dendrite trunk diameter.

A gradient freeze DS experimental set up consisting of a two zone resistance furnace on top, a hollow alumina insulating disk in the middle and a gallium cooling bath below was used to directionally solidify about 10 mm diameter Pb-5.8Sb alloy cylinders kept in evacuated quartz ampoules by heating the furnace to 650 co. and then cooling the hot zone at either at 0.5 °C/min or at 4 °C/min, while the bottom end of the sample was kept at room temperature by the water cooled gallium bath. Ten thermocouples were placed along the DS length to record the thermal profile as the liquid-solid interface traversed from the cold end to the hot end in response to the decreasing heat input from the top. The thermal profiles were used to estimate the thermal gradient and solidification speed at various locations along the sample length. Microstructures on the transverse sections were examined by cutting several 0.5 mm long transverse disks along the sample length. Morphology of primary dendrites was observed to change from being branch-less (cellular) in the very beginning of DS, to those showing onset of side-branching, and finally to well-branched tree-like structure having tertiary and higher-level side-branches as the solidification progressed from the cold to the hot end of the samples. Following conclusions can be drawn from this study.

Gradient Freeze DS method can be used to examine the morphological evolution of whole range of dendrite structures, from no branches to extensive branching, using one sample processed on the Space Station as compared with several required if one must use the steady state DS procedure.

Freckles (channel segregates) produced by “plume-type” thermosolutal convection are seen in the slower cooling rate sample, but not in the faster cooling rate

sample. These will not be present in the same alloy samples processed on the Space Station.

Extensive longitudinal macrosegregation of solute occurs during DS. The solidified sample, initially solute poor becomes increasingly solute rich along its length. The Space Station processed sample will be free of longitudinal macrosegregation.

The primary dendrite trunk diameter decreases, and the spacing, as measured by mean minimum spanning tree branch length or nearest neighbor spacing, increases during gradient freeze DS from one end of the sample to the other because of the changing thermal gradient and growth speed conditions along the DS length (The growth speed appears to increase and thermal gradient appears to decrease).

The experimentally observed primary spacing (minimum spanning tree and nearest neighbor spacing) values are less than those predicted from Hunt-Lu model. It is likely caused by the thermosolutal convection in the mushy-zone during DS of this alloy. A comparison with data from Space Station Processed samples will help us understand the role convection plays in reducing primary dendrite spacing.

Primary dendrite trunk diameter is larger in the samples than predicted from the analytical model which is based on side-branch coarsening under a diffusive mass transport conditions []. Again, a comparison with data from Space Station Processed samples will help us understand if convection does make trunk diameter coarser.

REFERENCES

1. Versnyder, F.L., Shank, M.E., The development of columnar grain and single crystal high temperature materials through directional solidification. *Materials Science and Engineering* 6, 213-247. 1970.
2. Kurz W, Fisher DJ. *Fundamentals of solidification*. Trans Tech, Aedermansdorf, 1986, p.77.
3. G.L. Ding, S.N. Tewari. Dendritic morphologies of directionally solidified single crystals along different crystallographic orientations. *Journal of Crystal Growth* 236 (2002) 420-428.
4. M.C. Flemings: in *Solidification Processing*, McGraw-Hill, New York, NY, 1974., pp.76-77.
5. M.H. Burden and J.D. Hunt. *Journal of Crystal Growth.*, 22(1974), 909-916.
6. M.D. Dupouy, D. Camel, and J.J. Favier. Natural convective effects in directional dendritic solidification of binary metallic alloys: dendritic array morphology. *Journal of Crystal Growth.*, 1993, vol. 126, pp. 480-88.
7. S.D. Felicelli, D.R. Poirier and J.C. Heinrich, Macrosegregation patterns in multicomponent Ni base alloys, *J. Cryst. Growth* 177, 145 (1997).
8. S.N. Tewari, R. Tiwari and G. Magadi, *Metallurgical and Materials Transactions A*, **35A** (2004) 2927-2934.
9. Ghods M, Johnson L, Lauer M, Grugel RN, Tewari SN, Poirier DR. Radial macrosegregation and dendrite clustering in directionally solidified Al–7Si and Al–19Cu alloys. *Journal of Crystal Growth*. 2016; 441:107-116. doi: <http://dx.doi.org/10.1016/j.jcrysgro.2016.02.014>.
10. S.N. Ojha, G. Ding, Y.Lu, J. Rye and S.N. Tewari, *Metallurgical and Materials*

- Transactions A*, **30A** (1999) 2167-2171.
11. S.N. Tewari and R. Tiwari, *Metallurgical and Materials Transactions A*, **34A** (2003) 2365-2376.
 12. R. Trevedi, Growth of dendritic needles from a supercooled melt, *Acta Metallurgica*, Volume 18, 1970, Pages 287-296.
 13. W. Kurz, D.J. Fisher, Dendrite growth at the limit of stability: tip radius and spacing, *Acta Metallurgica*, Volume 29, 1981, Pages 11-20.
 14. R. Trevedi, J. Lipton and W. Kurz, Effect of growth rate dependent partition coefficient on the dendritic growth in undercooled melts, *Acta Metallurgica*, Volume 35, 1987, Pages 965-970.
 15. V. Laxmanan. Dendritic solidification—I. Analysis of current theories and models, *Acta Metallurgica*, Volume 33, 1985, Pages 1023-1035.
 16. P. Lehmann, R. Moreau, D. Camel, R. Bolcato. A simple analysis of the effect of convection on the structure of the mushy zone in the case of horizontal Bridgman solidification. Comparison with experimental results, *Journal of Crystal Growth*, Volume 183, 1998, Pages 690-704.
 17. S.N. Tewari, R. Tiwari and G. Magadi, *Metallurgical and Materials Transactions A*, **35A** (2004) 2927-2934.
 18. J. Hunt and S. Lu, Numerical Modeling of Cellular/Dendritic Array Growth: Spacing and structure Predictions, *Metall. Mater. Trans. A*, vol. 27A, pp. 611-623, 1996.

19. S.N. Tewari, R.N. Grugel and D.R. Poirier, *Metall. Materials. Trans.* **45A** (2014) 4758-4761.
20. Metal Handbook, 8th ed., ASM Matal Park, OH, vol. 8, p. 329, 1961.